AGU PUBLICATIONS

JGR

Journal of Geophysical Research: Solid Earth

RESEARCH ARTICLE
10.1002/2014JB011489

Key Points:
- We analyze microstructures from SAFOD cores from the San Andreas Fault
- Pressure solution is the main creep process
- This process evolves with time, depth, and the distance to the gouge

Correspondence to:
J.-P. Gratier,
jean-pierre.gratier@ujf-grenoble.fr

Citation:
Richard, J., J.-P. Gratier, M.-L. Doan, A.-M. Boullier, and F. Renard (2014), Rock and mineral transformations in a fault zone leading to permanent creep: Interactions between brittle and viscous mechanisms in the San Andreas Fault, *J. Geophys. Res. Solid Earth*, *119*, 8132–8153, doi:10.1002/2014JB011489.

Received 29 JUL 2014
Accepted 20 OCT 2014
Accepted article online 28 OCT 2014
Published online 18 NOV 2014

Rock and mineral transformations in a fault zone leading to permanent creep: Interactions between brittle and viscous mechanisms in the San Andreas Fault

Julie Richard[1], Jean-Pierre Gratier[1], Mai-Linh Doan[1], Anne-Marie Boullier[1], and François Renard[1,2]

[1]ISTERRE, Université Grenoble Alpes and CNRS, Grenoble, France, [2]Physics of Geological Processes, University of Oslo, Oslo, Norway

Abstract Creep processes may relax part of the tectonic stresses in active faults, either by continuous or episodic processes. The aim of this study is to obtain a better understanding of these creep mechanisms and the manner in which they change in time and space. Results are presented from microstructural studies of natural samples collected from San Andreas Fault Observatory at Depth borehole drilled through the San Andreas Fault, which reveal the chronology of the deformation within three domain types. (i) A relatively undeformed zone of the host rock reflects the first step of the deformation process with fracturing and grain indentations showing the coupling between fracturing and pressure solution. (ii) Shear deformation development that associates fracturing and solution cleavage processes leads to profound changes in rock composition and behavior with two types of development depending on the ratio between the amount of dissolution and deposition: abundant mineral precipitation strengthens some zones while pervasive dissolution weakens some others, (iii) zones with mainly dissolution trended toward the present-day creeping zones thanks to both the passive concentration of phyllosilicates and their metamorphic transformation into soft minerals such as saponite. This study shows how interactions between brittle and viscous mechanisms lead to widespread transformation of the rocks and how a shear zone may evolve from a zone prone to earthquakes and postseismic creep to a zone of steady state creep. In parallel, the authors discuss how the creeping mechanism, mainly controlled by the very low friction of the saponite in the first 3–4 km depth, may evolve with depth.

1. Introduction

Active continental faults relax stress during short seismic events (earthquakes). They can also accommodate part of the deformation during periods of slow aseismic sliding by creep. Two types of creep can be distinguished. The first is a permanent steady state creep associated with specific properties of the fault rocks and their environment. In this case, deformation has a fairly constant strain rate [*Azzaro et al.*, 2001; *Burford and Harsh*, 1980; *Titus et al.*, 2006]. The second type of creep is recorded over periods ranging from months to decades after an earthquake; it can be considered as a postseismic creep process and occurs either in the lower crust below the seismic fault or in the upper crust around the seismic parts of the fault [*Barbot et al.*, 2009; *Gao et al.*, 2000; *Johanson et al.*, 2006; *Murray and Langbein*, 2006]. In the latter case, it is also referred to as an afterslip process [*Freed*, 2007; *Marone*, 1998].

Considering the relationships between aseismic deformation and fault processes, creep mechanisms need to be identified in order to gain a better understanding of the seismic cycle. Numerous observations have been made on ductile shear zones associated with major continental faults including the Great Glen Fault [*Stewart et al.*, 2000], the Outer Hebrides Fault Zone [*Holdsworth et al.*, 2002; *Imber et al.*, 2001], the Median Tectonic Line Fault in Japan [*Jefferies et al.*, 2006], the Red River Shear Zone [*Wintsch and Yeh*, 2013], the Longitudinal Valley Fault, Taiwan [*Lee et al.*, 2005; *Thomas et al.*, 2014; *Yu and Liu*, 1989], the Cléry fault in the Alps [*Gratier et al.*, 2013b], and the San Andreas Fault [*Steinbrugge and Zachery*, 1960; *Titus et al.*, 2006].

At least three major mechanisms that could weaken the faults and enhance creep deformation, or a combination of them, have been investigated.

1. The first is related to pore fluid overpressure [*Chester et al.*, 1993; *Etheridge et al.*, 1984; *Rice*, 1992; *Sleep and Blanpied*, 1992], and some studies have provided evidence of episodic fluid overpressure in the San Andreas fault core [*Holdsworth et al.*, 2011], but they also showed that this mechanism cannot explain

alone the weakness of this fault and its observed creep rate. Moreover, the potential sources of fluid in the fault do not provide a sufficiently high flux in order to maintain high fluid pressure [*Fulton and Saffer*, 2009; *Fulton et al*., 2009]. Such high fluid pressure events must be episodic and related to earthquake activity [*Mittempergher et al*., 2011] since at the present time no evidence of high fluid pressure was found in the San Andreas Fault Observatory at Depth (SAFOD) borehole [*Zoback et al*., 2011].

2. The second deformation mechanism is frictional sliding. In order to fit the observed low heat flow along the San Andreas Fault creeping zone, a large amount of very weak minerals is required, such as talc, smectite, and other low-friction clays. It is often postulated that when distributed along an interconnected slip surface network, a relatively small amount of weak minerals (10–20%) may significantly lower the friction [*Collettini et al*., 2009a; *Handy*, 1990]. However, if friction occurs along nonoptimally oriented surfaces, like some of those in the interconnected network, this could lead to an effective friction of the mixed material higher than the intrinsic friction coefficient of the weak minerals. The effective friction could be higher than the very low friction value required to explain the absence of heat along certain creeping zones such as the San Andreas Fault [*Brune et al*., 1969; *Lachenbruch and Sass*, 1980]. Consequently, this mechanism depends both on rock composition and on the temperature and pressure conditions [*Carpenter et al*., 2009, 2011; *Collettini et al*., 2009a; *Moore and Rymer*, 2007; *Moore and Lockner*, 2011; *Lockner et al*., 2011; *Tembe et al*., 2010]. Laboratory experiments also suggest that low friction is correlated to velocity-strengthening behavior that inhibits the nucleation of earthquakes [*Ikari et al*., 2011].
3. Finally, the last creeping process that could accommodate large aseismic deformation without heat production is pressure solution creep [*Gratier et al*., 2011; *Holdsworth et al*., 2011; *Rutter and Mainprice*, 1979; *Schleicher et al*., 2009b]. This deformation mechanism is a stress-driven fluid-assisted mass transfer process, widely recognized in the rocks of the upper crust [*Gratier et al*., 2013a, and references therein]. Due to local variations in chemical potential related to local stress heterogeneities, soluble minerals (such as quartz, feldspar, and serpentine) are progressively dissolved, transferred along a fluid phase trapped under stress and either precipitated or washed away when reaching open pores [*Paterson*, 1973; *Weyl*, 1959]. This leads to a passive concentration of insoluble minerals (such as phyllosilicates and oxides) in the dissolution zones. Such chemical segregation leads to the development of a foliation perpendicular to the direction of the maximum normal stress, consequently expressing a ductile deformation of the rock by spaced or slaty cleavage [*Hobbs et al*., 1976; *Ramsay*, 1967; *Siddans*, 1972; *Wood*, 1974] or by superplastic deformation [*Ashby and Verall*, 1973] with pressure solution diffusion-accommodated grain sliding [*Gratier et al*., 2011].
4. Moreover, it has been suggested from both experiments and natural observations that frictional and pressure solution mechanisms could be associated in accommodating sliding as a frictional-viscous creep mechanism [*Bos and Spiers*, 2002; *Bos et al*., 2000; *Jefferies et al*., 2006]. This model will be discussed in relation to the superplasticity model on the basis of the geometry of the sliding pattern.

Another major issue in the study of creeping faults is the fact that fault rocks may transform with time and space through various processes. (a) Pressure solution can lead to the concentration of insoluble species, such as phyllosilicates, that can be localized along the planar connected network, thereby facilitating frictional sliding [*Collettini et al*., 2009b]. (b) Fluid flow can enhance metamorphic transformation leading to the development of low friction minerals [*Moore and Rymer*, 2012]. (c) Fluid flow of reactive undersaturated solutions can enhance the permeability of the rocks along localized self-organized high permeability paths [*Ortoleva and Chen*, 1990]. (d) Microfracturing may be associated with the creeping zone [*Rubin et al*., 1999] and is found to accelerate pressure solution creep in the laboratory [*Gratier et al*., 2014]. (e) Healing of the fractures either by self-healing [*Brantley et al*., 1990; *Li et al*., 2006] or by precipitation sealing [*Ramsay*, 1967] strengthens the rocks. (f) Processes of fracturing and coupled dissolution-precipitation reactions also create or destroy porosity and are responsible for slow deformations in the middle to upper crustal rocks [*Cox and Etheridge*, 1989].

The aims of this study are to obtain a better understanding of these creep mechanisms and how they change in time and space and to evaluate the key parameters of the transformation. The original contribution of the study is to show the possible change in deformation with time with considerable transformation of the rocks, with regard to both their composition and their structure. This change in composition and structure is studied through the identification of deformation mechanisms, based on new microstructural observations, and on data already published in other papers [*Gratier et al*., 2011; *Hadizadeh et al*., 2012;

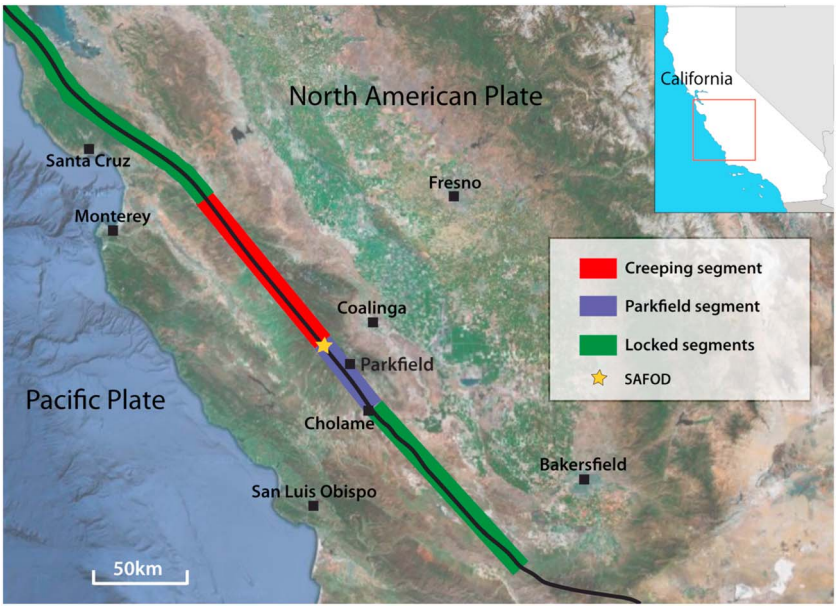

Figure 1. Location map of the San Andreas Fault (SAF) and SAFOD borehole in central California, displaying also the different fault segments.

Holdsworth et al., 2011; *Janssen et al.*, 2010, 2012; *Mittempergher et al.*, 2011; *Schleicher et al.*, 2009a, 2010; *Solum et al.*, 2007; *Zoback et al.*, 2010]. To the author's knowledge, this time-dependent change has never been discussed in such detail up till now.

For this purpose, dozens of samples retrieved from the San Andreas Fault Observatory at Depth (SAFOD) borehole were studied. The comparison of all these samples gives clues to understand how the fault zone has evolved. Based on the example of the San Andreas Fault, the manner in which a plate boundary shear zone may evolve from a zone with earthquakes and postseismic (afterslip) relaxation to a zone of steady state creep is postulated.

2. San Andreas Fault and SAFOD Borehole

2.1. Geological Setting and General Features

The San Andreas Fault (SAF) system, California, is a complex network of faults extending over 1300 km in length and 100 km width [*Wallace*, 1990], forming the junction between the subducting Pacific Plate and the North American Plate. The SAF is the major continental fault of this network, and one of the most studied faults in the world. It is generally accepted that the modern SAF has been the principal transform fault for the last 5 Myr but that other faults in the San Andreas system have also accommodated relative motion along the plate boundary for more than 20 Myr [*Powell*, 1993; *Powell and Weldon*, 1992; *Weldon et al.*, 1993]. The pre-late Cenozoic rock units have a structural pattern that is transected obliquely by the right lateral system of the SAF [*Powell*, 1993], and continental block rotations were associated with the dextral shear regime [*Nicholson et al.*, 1994]. The modern SAF is a lithospheric mature dextral strike-slip fault divided into different segments with varying mechanical behaviors [*Allen*, 1968; *Irwin and Barnes*, 1975; *Steinbrugge and Zachery*, 1960; *Wallace*, 1970]. The creeping segment (Figure 1) is currently experiencing a continuous aseismic slip at a rate ranging between about 28 mm/yr and 33 mm/yr [*Burford and Harsh*, 1980; *Titus et al.*, 2006], which is close to the 34 mm/yr long-term estimated geological slip rate [*Sieh and Jahns*, 1984], and exhibits a high microseismic activity [*Nadeau et al.*, 2004; *Provost and Houston*, 2001]. The creeping zone is bounded along-strike by locked segments that have experienced some infrequent earthquakes of large magnitude, such as the Fort Tejon earthquake in 1857 ($M = 7.9$) [*Sieh*, 1978] on the southern locked segment and the San Francisco earthquake in 1906 ($M = 8.2$) on the northern locked segment. The locked segments are also characterized by negligible or nonexistent creep [*Ellsworth*, 1990]. Finally, the Parkfield segment forming the junction between the creeping segment and the southern locked segment (Figure 1) has a transitional behavior. This segment has experienced seven

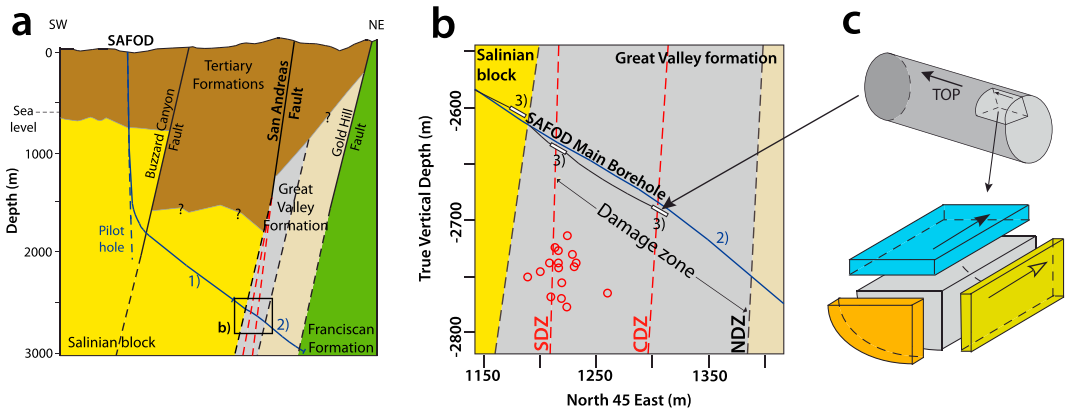

Figure 2. (a) Simplified NW-SE geological cross section of the SAFOD borehole area and its intersection with the SAF: Salinian block (yellow) with granitoid rock west of the Buzzard Canyon fault and arkosic sandstone east of this fault, Tertiary sediment (brown), Cretaceous Great Valley formation (gray and light brown), and Cretaceous Franciscan formation (green). Dashed red lines indicate the two active creeping zones (Southwest Deforming Zone (SDZ) and Central Deforming Zone (CDZ)) [after *Zoback et al.*, 2010]. A black square delineates the area focused in Figure 2b. (b) Simplified cross section of the SAFOD main borehole, location of the sidetrack boreholes used to obtain core samples during Phase 3, in the damaged zone area [after *Zoback et al.*, 2011] and location of microseismicity (red circles); (c) sketch representing the orientation and position of the samples studied relative to the oriented core. Thin sections of those samples were cut according to the three directions represented by the colored sections (blue, green, and yellow). The blue and green sections are parallel to the hole and perpendicular to the fault and consequently to the foliation, while the yellow section is perpendicular to the hole and parallel to the foliation.

repeating earthquakes of magnitude close to 6 since 1857 [*Bakun and McEvilly*, 1984; *Jackson and Kagan*, 2006], a transitory postseismic creep episode after the last 2004 event [*Titus et al.*, 2006] and an intense microseismic activity [*Thurber et al.*, 2004].

The fault crosses different geological formations, and given the tectonic setting of subduction, the geographical distribution of these formations is not symmetrical on both sides of the fault, especially in the Parkfield area (Figure 2), where the present study is focused. The structure of the fault itself is complex and presents major heterogeneities at depth, with some formations intensively deformed like the Franciscan Complex, and the presence of a large body of serpentine close to the Parkfield segment [*Andreani et al.*, 2005; *Li et al.*, 2004; *McPhee et al.*, 2004; *Moore and Rymer*, 2012]. Away from the fault, the regional deformation of the Franciscan Complex, which can be related to the subduction [*Page et al.*, 1998], is preserved as an anastomosing cleavage that wraps around massive blocks with an overall moderate average dip of 45° to the NNE [*Andreani et al.*, 2005]. Conversely, the dense cleavage in the San Andreas damage zone and in the gouge, which is oriented near-parallel to the fault, is vertical and is consistent with the present-day dextral wrench movement of the fault. Studies have also revealed some very specific features in the geophysical and mechanical properties of the SAF. The discovery that there is no heat flux anomaly across the creeping segment [*Brune et al.*, 1969; *Lachenbruch and Sass*, 1980] indicates that this fault slides with a much lower shear stress than that predicted by laboratory friction experiments [*Byerlee*, 1978]. This discovery, popularly known as the San Andreas stress-heat flow paradox [*Hanks and Raleigh*, 1980; *Lachenbruch and Sass*, 1992; *Zoback et al.*, 1988], has raised at a very early stage the question of potential mechanisms that can produce creep, without heat production. Moreover, *Mount and Suppe* [1987] and *Zoback et al.* [1987] provided evidence showing that the orientation of the maximum horizontal compressive stress is at a high angle to the fault. This angle increases with depth and ranges from 25° to 69° between 1000 m and 2200 m depth [*Hickman and Zoback*, 2004]. All these observations point to a weak fault embedded in a strong crust [*Boness and Zoback*, 2004; *Chéry et al.*, 2004; *Fulton et al.*, 2004; *Rice*, 1992; *Townend and Zoback*, 2004; *Zoback et al.*, 1987; *Zoback*, 2000; *Zoback et al.*, 2010].

When considering the morphology of such a strike-slip fault, a major difficulty is to access the fault core material. The information on the physical and chemical mechanisms acting at depth are difficult to get from outcropping rocks: fault cores are notoriously badly exposed, the information on the in situ fluids are most often lost, and surface processes such as weathering do have the capacity to badly degrade the exposed fault rocks. Drilling directly through the fault was considered to be the best way of studying the fault processes in situ [*Zoback et al.*, 2010].

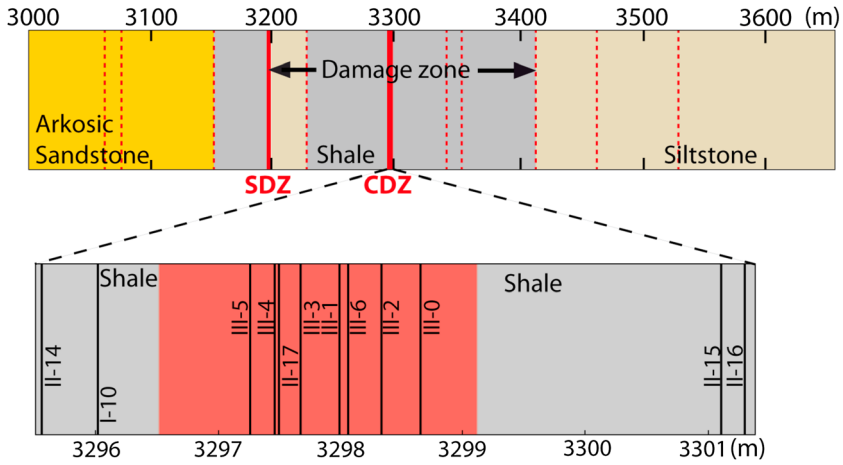

Figure 3. Location of the samples studied in a schematically represented part of the main hole. The measured depth values are relative to Phase 3 Core. Colors show the different rock formations, vertical red bars indicate the places where the steel casing is actively deforming, and dotted red lines mark the faults crossed by the borehole. The black lines show the location of the samples in the creeping zone. The location of the other samples is given in Table 1.

2.2. SAFOD Borehole

The San Andreas Fault Observatory at Depth (SAFOD) drilling project aimed to provide in situ geophysical borehole data and fault core samples, to obtain a more accurate idea of the fault rock properties, the conditions for earthquake nucleation, and to find an explanation for the San Andreas stress/heat flow paradox [*Hickman et al.*, 2007; *Zoback*, 2006; *Zoback et al.*, 2011]. The borehole was drilled close to the town of Parkfield (Figure 1), on the eponymous fault segment and reached 3 km vertical depth (Figure 2a). This site was chosen because of its location at the transition between two segments having different mechanical behavior and the presence of patches of repeating microearthquakes located between 2 km and 12 km depth within an aseismic creeping zone [*Nadeau et al.*, 2004; *Zoback et al.*, 2010] (Figure 2). The main borehole was drilled in three phases between summer 2004 and summer 2007 [*Zoback et al.*, 2011]. In its upper part, the NE-dipping Phases 1 and 2 borehole (Figures 2a and 3) crosses a thick sequence of arkosic sandstones and conglomerates belonging to the Pacific Plate, which are relatively undeformed [*Draper-Springer et al.*, 2009]. Then an abrupt change in lithology is observed at 3157 m MD (Measured Depth relative to Phase 2), with a sequence of fine-grained shales and siltstones [*Bradbury et al.*, 2007] that passes at greater depths (below 3400 m MD) into a siltstone-claystone sequence that are identified as Cretaceous Great Valley Group based on their texture, composition, and the presence of Late Cretaceous Great Valley fossils [*Draper-Springer et al.*, 2009]. From 3187 to 3413 m (Figures 2b and 3), a 200 m wide region is characterized by a decrease in the velocity of *P* and *S* waves and by its low resistivity, compared to the other sections of the borehole [*Jeppson et al.*, 2010; *Zoback et al.*, 2011] and is called the damage zone [*Zoback et al.*, 2010, 2011]. This damage zone is mainly composed of siltstones, mudstones, shales [*Bradbury et al.*, 2007; *Schleicher et al.*, 2009a; *Solum et al.*, 2007], and very fine grey sandstones of the Great Valley sequence [*Holdsworth et al.*, 2011]. Three zones of particularly low velocity and resistivity can be identified at 3192 m (SDZ), 3302 m (CDZ), and 3413 m (NDZ) (Figures 2b and 3). The Phase 3 of the drilling process included the recovery of about 40 m of 10 cm diameter rock core from three key sections (Figure 2b): the sandstones of the Salinian block near the boundary of the damage zone and the areas of the SDZ and the CDZ creeping zones. The SDZ and more largely the CDZ are characterized by ongoing deformation of the steel casing inside the borehole, indicative of active creeping processes. The first zone, the SDZ, is located between 3196 m and 3198 m depth (depths are given here relative to Phase 3 Core, see Table 1 for the equivalence between the different depth location systems). This is the less active zone. The CDZ, located between 3296.5 m and 3299 m depth (relative to Phase 3 Core), is the more active deforming zone. The active creeping zones are mainly composed of phyllosilicate minerals (mainly clays as saponite) with serpentine clasts as well as lithic clasts coming from siltstone and mudstone rocks, similar to those composing the fault rocks at the boundaries of the creeping zone [*Holdsworth et al.*, 2011; *Moore and Rymer*, 2012]. Several

Table 1. Overview of the Location of the Samples Studied Listed With Increasing Depth Along the Borehole (MD) in SAFOD[a]

Core Section	Phase 2 (m)	MD Phase 3 (m)	Samples
E11		3141.82	I-1*
E12		3142.71	I-2
E12		3142.98	I-3
E13		3143.57	I-5*
E13		3144.12	I-4
E16		3146.34	I-6
E17		3147.36	I-8
G12a		3187.6	II-11*
G12b		3187.9	II-12*
G23		3192.9	II-13
G21		3193.48	II-19*
G24		3193.99	I-7*
G25		3194.97	II-20*
SDZ top	3191.407	3196.44	
G28		3197.2	II-18*
SDZ bottom	3193.023	3198.05	
G31a		3198.6	I-9A*
G31b		3198.7	I-9B*
G41		3295.56	II-14
G42		3296.04	I-10*
CDZ top	3300.524	3296.56	
G43		3297.27	III-5*
G43		3297.48	III-4
G43		3297.49	II-17
G44		3297.68	III-3
G44		3297.99	III-1
G44		3298.06	III-6
G44		3298.34	III-2
G45		3298.65	III-0
CDZ bottom	3303.084	3299.12	
G51		3301.17	II-15
G52		3301.32	II-16
G54		3303.82	II-21*

[a]The Core Section column gives information on side-track boreholes (G43 stands for hole G, Run 4, section 3). All the samples presented here come from Phase 3. In the denomination of samples (the column Samples), the first number indicates the Round of sample requests (II-14 stands for Round II, sample no. 14 of the sample set received from this Round). As the Phase 3 core consists of a series of boreholes side-tracking the Phase 2 hole, the measured depths can vary depending on the hole considered. *Zoback et al.* [2010] give the methodology for correlating the values of the measured depths of Phase 3 with those of Phase 2. Here for the values of the core section of Hole G, Runs 4–6, a value of 3.96 m needs to be added to the Phase 3 measured depths to obtain the corresponding depth with Phase 2. The two columns, MD Phase 2 and MD Phase 3, give the corresponding values in meters of measured depth of our samples, taking into account this correction, as well as the location of the top and bottom of the CDZ. The correspondence with the nature and the structure of the rocks may be seen in the cross sections of Figures 2 and 3. Asterisks indicate samples that have been studied previously [*Mittempergher et al.*, 2011; *Gratier et al.*, 2011; *Hadizadeh et al.*, 2012].

samples of the active creeping zones were used for testing experimentally the friction coefficient of those creeping zones. *Lockner et al.* [2011] and *Carpenter et al.* [2011] both found low values of the friction coefficient ranging from 0.16 and 0.21. These results support the model of a weak fault in an otherwise strong crust. Various observations have been made on the natural samples with a view to understanding creep mechanisms [*d'Alessio et al.*, 2006; *Gratier et al.*, 2011; *Hadizadeh et al.*, 2012; *Holdsworth et al.*, 2011; *Janssen et al.*, 2010, 2012; *Moore and Rymer*, 2007; *Schleicher et al.*, 2009a, 2010; *Solum et al.*, 2007; *Zoback et al.*, 2010]. The study by *Holdsworth et al.* [2011] proposed that the cores can be most conveniently divided into three domain types: (a) Relatively undeformed host rocks that can be found in all the sandstones east of the damage zone boundary, and in part of the CDZ area; (b) pervasively sheared regions of presently 'inactive' (not creeping) fault rocks in most of the SDZ area; and (c) narrow, pervasively sheared regions of actively creeping fault rocks, corresponding to the SDZ and CDZ creeping zones. This classification has been adopted here to describe the sample microstructures below.

3. Microstructure Observations in the San Andreas Fault Zone

3.1. Location and Preparation of the Samples

During the three rounds of sample requests, several samples were collected to characterize the typical microstructures found in the SAFOD fault zone. Figure 3 shows the location of the samples studied. The measured depths are relative to Phase 3 Core (see Table 1). Most of these samples were impregnated with epoxy resin and cut into thin sections. At least three thin sections of each sample were made along three perpendicular directions relative to the core top (Figure 2c). In the first stage an optical microscope was used to determine the general features. These observations provided an initial compilation of the most representative thin sections for each sample, on which scanning electron microscopy (SEM) observations, cathodoluminescence, and chemical mappings were carried out. A second selection based on this analysis was made in order to focus on several thin

sections subjected to Field Emission Gun scanning electron microscopy (FEG-SEM energy-dispersive X-ray analyses and chemical maps for the three domain types). X-ray powder diffraction analyses on fragments were collected to determine the overall mineralogical composition of the various domains.

3.2. Sample Observations

These samples are representative of the three domain types discussed above [*Holdsworth et al*., 2011]. To study the deformation microstructures and mineral composition and to characterize their spatial changes, a classification integrating the mechanisms of deformation is used. The "Fractured and indented structures" class is used for the relatively undeformed rocks. "Fractured and foliated shear zones" is used for the shear zones. "Grain sliding accommodating active creep" is used for the present-day active creeping zone and is focused mainly on the CDZ.

3.2.1. Fractured and Indented Structures (Relatively Undeformed Zones)

These relatively undeformed zones are found outside the damage zones in the arkosic sandstones 3140 m to 3160 m (Figure 3) and in the damage zone as locally protected or strengthened relics of the host rocks (Figures 2b and 3).

Most of the grains, and more specifically quartz and feldspar grains, are highly fractured (Figure 4). The fractured grains show multiple radial fracturing in a fan-like shape rooted at the contact between the grains. It is also possible to observe widespread indentations between grains of different or similar nature (Figures 4a and 4b). For example, at the contact between a feldspar and a quartz grain, a chemical differentiation is observed (Figures 4d and 4e). The passive concentration of insoluble species (Fe, Mg, K, and Ti) corresponding to small phyllosilicates and Ti-Fe oxides that are trapped in contact between the grains is indicative of the stress-driven feldspar dissolution (Figure 4e).

Several microfaults to mesofaults may be identified in relatively undeformed zones [*Hadizadeh et al*., 2012; *Holdsworth et al*., 2011; *Schleicher et al*., 2009b; *Solum et al*., 2006], with displacement ranging from micrometers to centimeters. Some typical structures may be seen associated with these faults: blocky textures of calcite reflecting euhedral growth in open voids are observed in association with anhydrite and local intrusion of sheared shale into the veins (sample I-9, *Mittempergher et al*. [2011], location in Table 1). The small fault gouges are also zones of quartz and feldspars dissolution that induces passive concentration of insoluble species (Fe, Mg, K, and Ti) corresponding to phyllosilicates and Ti-Fe oxides (Figure 3, sample I-1, *Hadizadeh et al*. [2012], location in Table 1). Broadly speaking, the internal mean strain values associated with both microfracturing (excepting large fault sliding) and pressure solution indenting remain very low in such relatively undeformed zones. The low strain nature of these rocks is backed up by the very widespread preservation of little deformed and often quite delicate sedimentary structures (bedding, lamination, grading, convolute bedding, bioturbation features, and fossils [*Holdsworth et al*., 2011]). Shortening strain values (l_s/l_0) of a few percent can be estimated (l_s = final; l_0 = initial length). Assuming bulk simple shear strain, this corresponds to very low shear strain (γ) values, close to 0.1 [*Ramsay*, 1967].

3.2.2. Fractured and Foliated Shear Zones

Part of the damage zone is both foliated and fractured with zones of relatively extensive deformation, referenced by *Holdsworth et al*. [2011] as "inactive gouges." Pervasive foliation is the main deformation pattern in such shear zones (Figure 5). Some of these shear zones are located just at the boundary of the present creeping zone (Figure 3). Others are located throughout the damage zone. The foliation is mainly linked to pressure solution cleavage associated with tectonic layering (Figures 5c–5e). The layering associates (i) zones of dissolution depleted in quartz, feldspar, or calcite and enriched with phyllosilicates and Ti-Fe oxides and (ii) zones that are either representative of the initial state or that are enriched with calcite precipitated in veins perpendicular to the cleavage (Figure 5e). The amount of total mass decrease at the level of each pressure solution cleavage seam may reach −90% on those foliated areas, based on the quantification of the proportional decrease in mass of each mineral that almost totally disappeared in these dissolution zones [*Gratier et al*., 2011]. Such foliation is observed at different scales, from the size of a grain to decimeters in the shear zones [*Hadizadeh et al*., 2012; *Mittempergher et al*., 2011]. When looking carefully at the chemical maps, it can be seen that the foliation is made of cleavage surfaces lying at various angles, and cross cutting each other, as is the case when cleavages develop in a shear zone (Figure 5) [*Gratier et al*., 2011]. Near the boundary of the CDZ, such shear zones are oriented nearly parallel to the creeping zone. Near the SDZ, tectonic layering is seen to develop at the scale of rigid objects: the foliation is bent around the

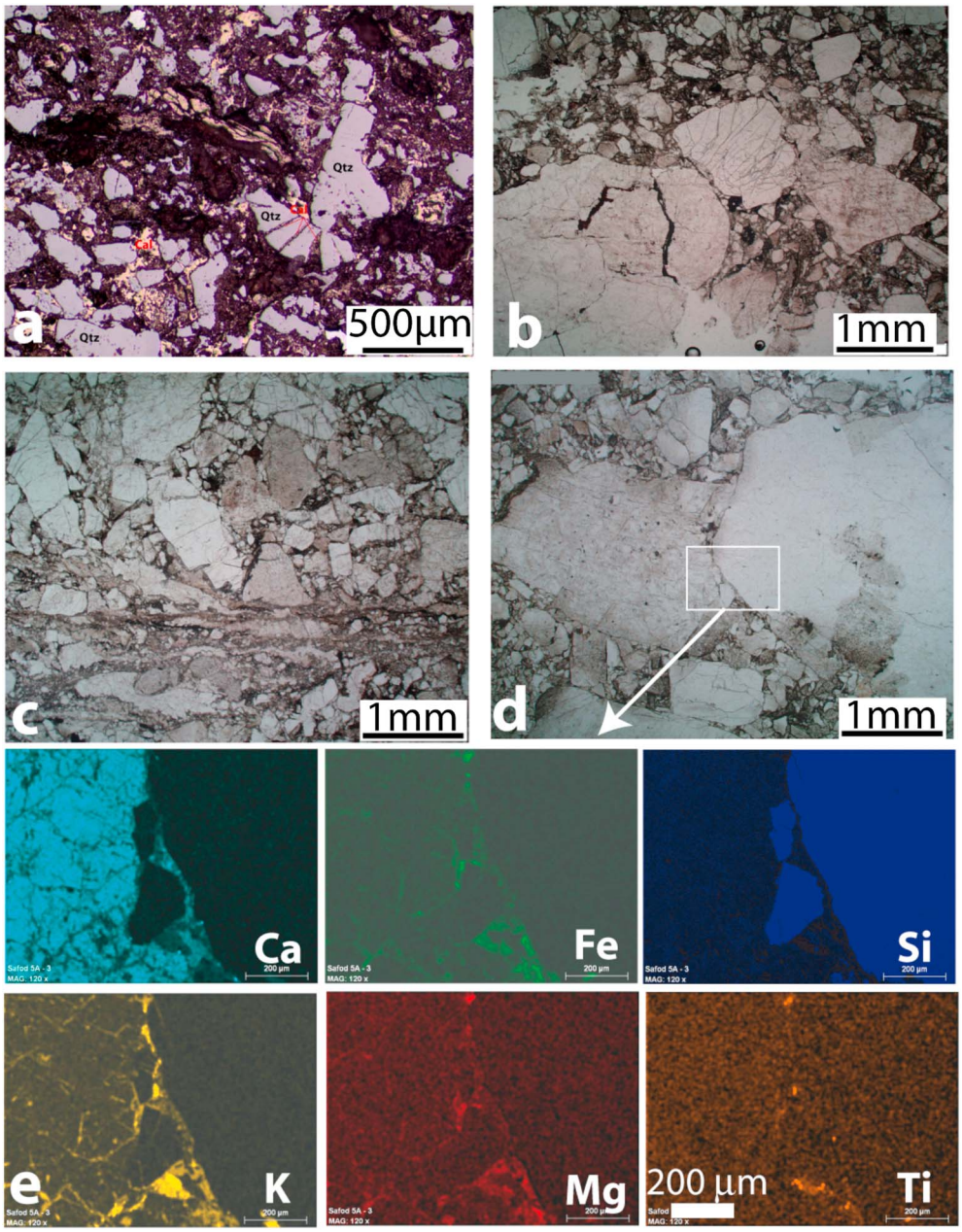

Figure 4. Main microstructural features observed in thin sections in the samples located in relatively undeformed zones with fracturing and indenting. (a) Optical microscope picture showing dynamic fracturing with radial cracks (sample I-10). (b and c) Optical microscope pictures showing the general intense fracturing of the material as well as the indentations (samples I-1 and I-3). (d) Optical microscope picture with an example of the numerous indentations between quartz and feldspar grains (sample I-5). (e) Elements distribution from scanning electron microscopy (SEM) at grain contact, brighter color indicates the higher the content. The passive concentration of several elements (Fe, Mg, and Ti) that belong to insoluble minerals (phyllosilicates and oxides) underlines pressure solution indentation, location of the map on the image of Figure 4d.

rigid objects with a clear depletion of Ca Na, K and Si and enriched in Fe and Mg relative to the less deformed shale located in the pressure shadows of the rigid object (reflecting the initial state since there is no evidence of secondary precipitation here) [*Gratier et al.*, 2011, Figure 2; *Mittempergher et al.*, 2011, Figure 2, Samples 1–9]. It should be noted that the zone of maximum deformation around the rigid object is associated with a decrease in grain size relative to the initial state best preserved in the pressure shadow. Broadly speaking, the internal mean strain values associated with the pressure solution cleavage are relatively high with shortening strain values (l_s/l_0) up to 0.4. This could correspond to a shear strain (γ) of up to 2 [*Ramsay*, 1967].

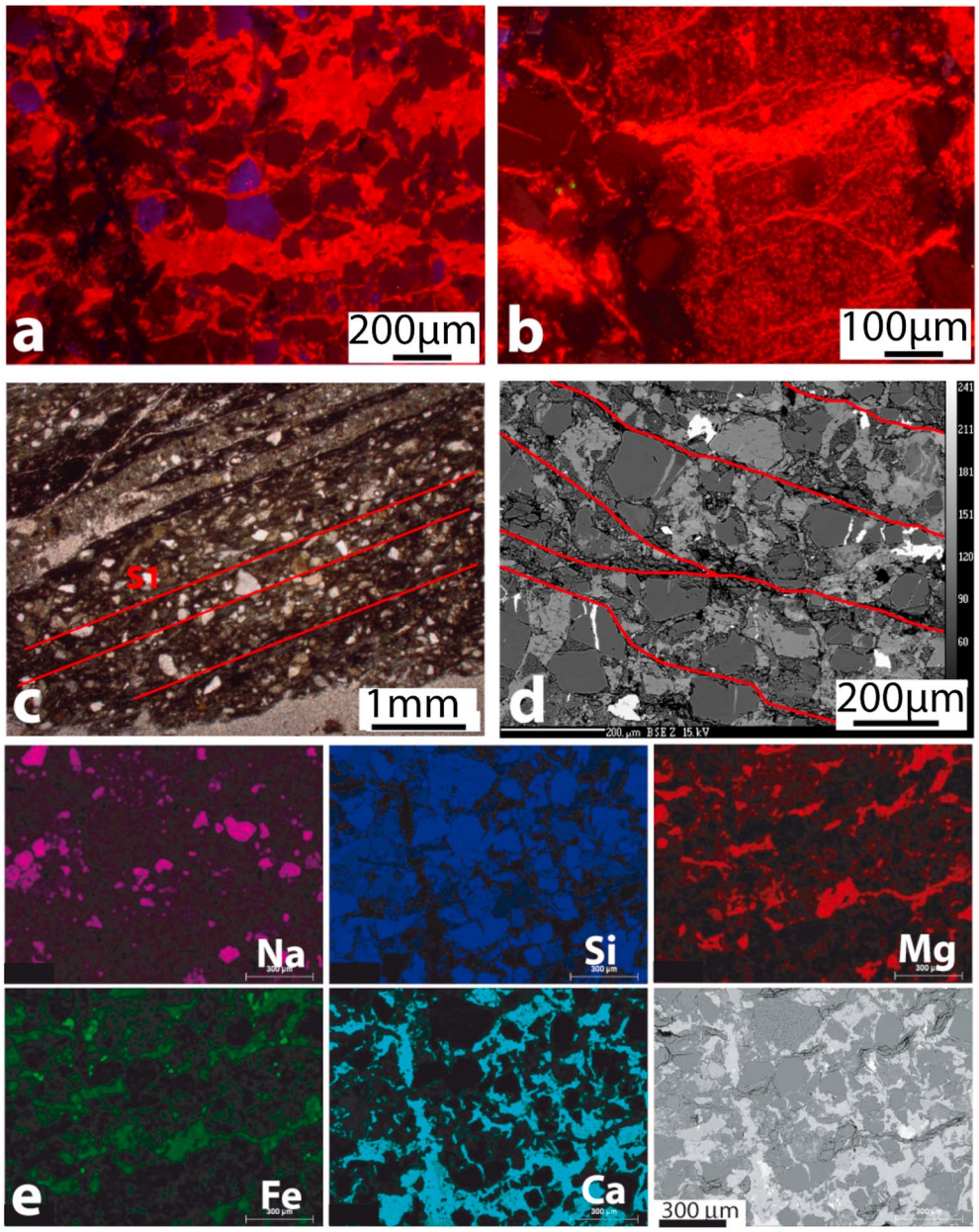

Figure 5. Main microstructural features observed in thin sections in the samples located in deformed zones with fracturing and foliated structures. (a and b) Cathodoluminescence images showing the well-developed calcite vein network in bright red, at different scales. The minerals in blue are feldspars, and the dark brown ones are quartz (sample I-9). (c) Optical microscope picture presenting an example of foliation developed by pressure solution mechanism (sample II-14). (d) backscattered electron analysis (BSE) image showing solution cleavages at the grain scale (sample I-10). (e) Elements distribution from scanning electron microscopy (SEM) in deformed zone with solution cleavage and veins (sample I-10), brighter color indicates the higher the content. The passive concentration of several elements (Fe, Mg, and Ti) that belong to insoluble minerals (phyllosilicates and oxides) underlines pressure solution cleavage that contributes to a tectonic layering process.

Networks of numerous calcite veins can be easily identified (Figures 5a and 5b). They may be seen at various scales from the size of a grain when sealed fractures are perpendicular to pressure solution cleavages (Figure 5), to decimeters when a large network of veins is present without solution cleavage. In the latter case, the layering is at decimeter scale, with alternating zones of pressure solution foliation (depleted in soluble quartz, feldspar, and calcitic minerals) and elements of host rock with a network of large calcitic veins that lie in every direction, as is the case when deformation evolves with time in shear zones [*Gratier et al.*, 2013a]. Broadly

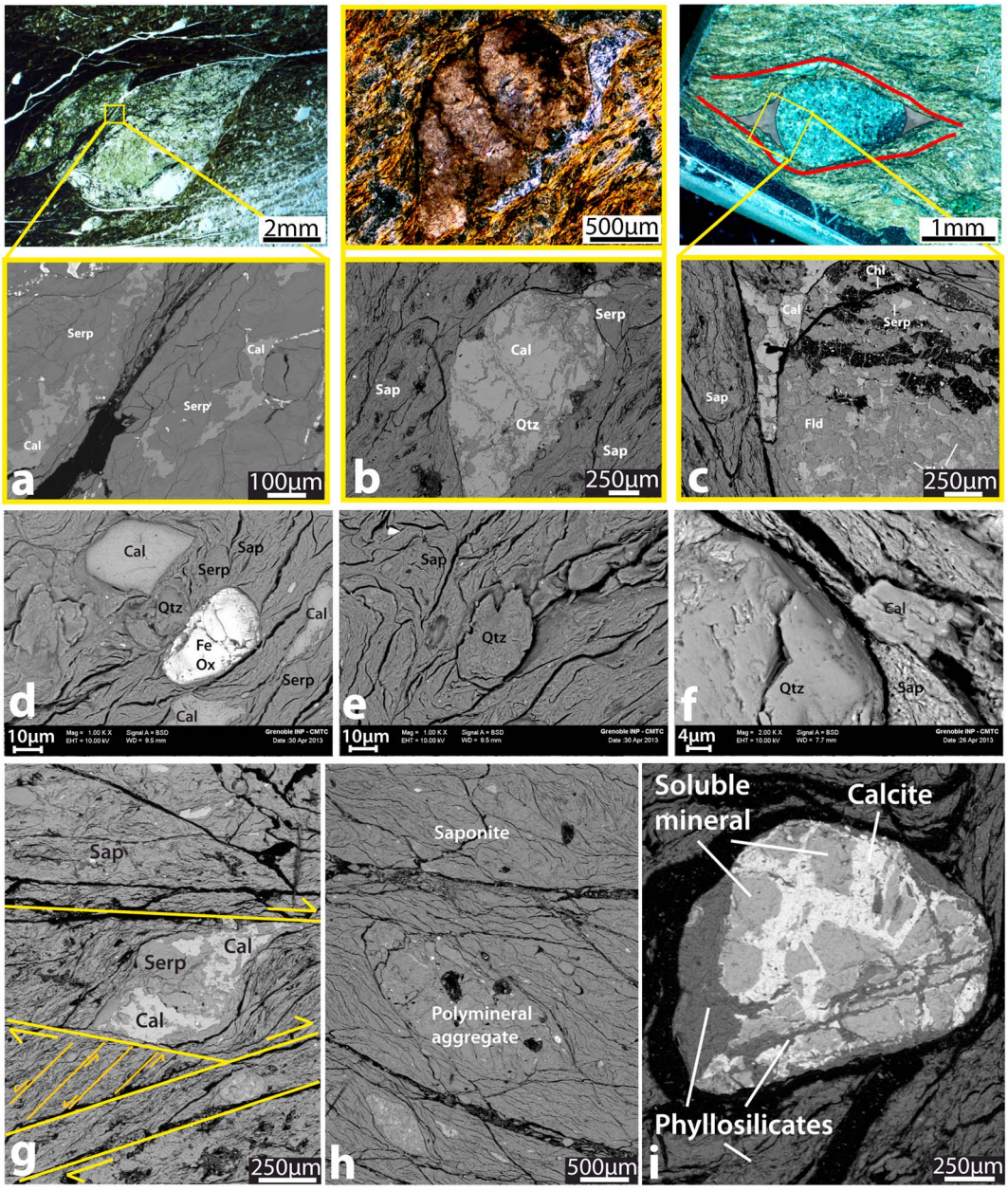

Figure 6. Main microstructural features observed in thin sections of samples located inside the active creeping zone with grain sliding accommodating the creep. (a–c) Top: color optical microscope pictures presenting some examples of polymineral clasts. Bottom: Microprobe BSE images (in black and white) show the differences in mineral composition between these aggregates (samples III-4, III-6, and III-0). (d–f) FEG-SEM BSE images showing examples of small grains presenting evidence of pressure solution at their edges. They also show the abundance of very small grains (<10 µm) inside the clay matrix, forming the creeping zone material (samples III-4, III-4, and III-0). (g–i) SEM BSE images displaying the multiple shear planes and their various orientations (yellow lines), as well as the very disturbed foliation inside the thin shear planes. Qtz: quartz, Cal: calcite, Serp: serpentine, Fld: feldspar, Chl: chlorite, Sap: saponite, Fe ox: iron oxide (samples III-0, III-3, and II-17).

speaking, the internal mean strain values (l_e/l_0) associated with these veins vary from near 0 up to 2. Assuming bulk simple shear deformation, this could correspond to shear strain (γ) values of up to 2 [*Ramsay*, 1967].

Observations of the geometry of the calcite growth give information on the relative kinetics of the fracture opening and sealing [*Bons*, 2001]. Some veins are filled with calcite fibers with crack seal growth indicative of a near continuous small opening (some tens of microns wide) and sealing probably associated with local solution cleavage. Conversely, other veins are filled with blocky euhedral-shaped crystals that provide

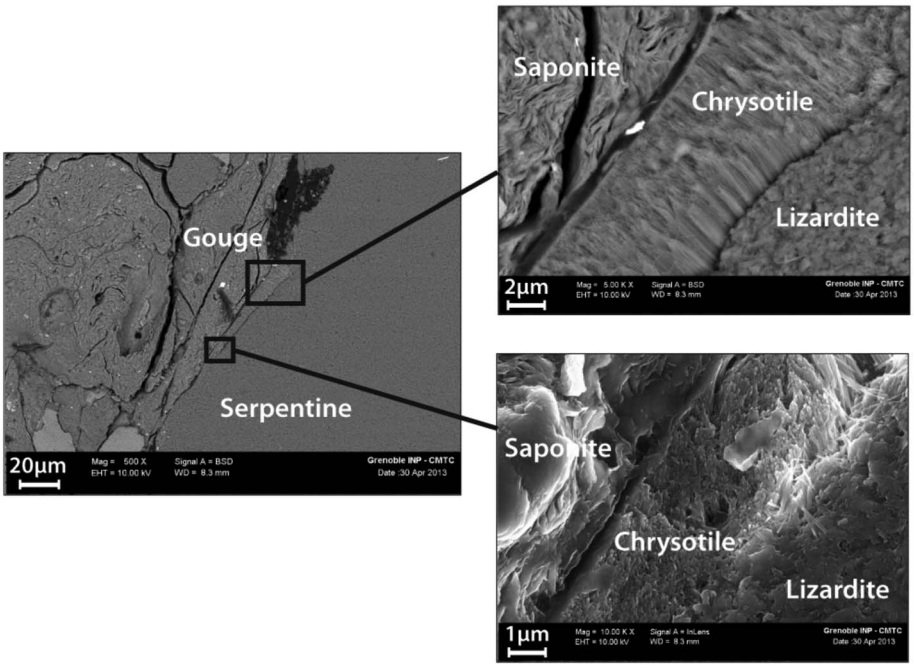

Figure 7. Samples located inside the active creeping zone with grain sliding accommodating the creep: examples of two different serpentines. The three pictures are FEG-SEM images, taken from sample III-0 at the boundary between an aggregate mainly composed of serpentine and saponite clay. Most of the serpentine forming clasts or present in the aggregates is lizardite. Chrysotile is located mainly along the boundaries of the serpentine aggregates or clasts, as here.

evidence of a widely open vein and calcite growth in free fluid. Studies in cathodoluminescence reveal the different luminescence colors of the calcite highlighting variations in minor elements content (Fe versus Mn) showing various fluid compositions during growth. As for other minerals, the calcite grains filling the veins are highly fractured in some areas, indicating changing deformation rates with time (Figure 5), with occasionally near continuous (creep) and occasionally episodic (earthquake) deformation. Earthquakes that occur on neighboring faults can produce the brittle damage observed along the studied rocks.

3.2.3. Grain Sliding Accommodating Active Creep (Actively Creeping CDZ Zone)

For the samples inside the creeping zone (Figure 6), rock composition is the main difference compared to the host rocks and to most of the fractured and foliated domains in the sheared zone. The CDZ is much richer in phyllosilicates (up to 50 or even 70%) than most of these rocks which contain less than 10% [*Solum et al.*, 2006] with the exception of certain localized dissolution zones in the foliated shear zones that may also have a very high content in passively concentrated phyllosilicates (up to 50 or even 90%) [*Gratier et al.*, 2011]. However, compared to these highly phyllosilicate-rich shear zones, another notable difference is the nature of the phyllosilicates. In the shear zones, phyllosilicates are mainly chlorites. In the CDZ, X-ray diffraction analyses show that the phyllosilicates belong to the Mg-rich smectite group (saponite) [*Holdsworth et al.*, 2011; *Lockner et al.*, 2011; *Moore and Rymer*, 2012; *Schleicher et al.*, 2009a]. These results are confirmed by SEM, X-ray diffraction, and microprobe chemical analysis [*Richard*, 2013].

Another typical feature is the presence of polymineral clasts of various sizes, ranging from 10 µm to the diameter of the core sample (10 cm) (Figure 6) and possibly much larger. Their composition is very close to that of the rocks outside the CDZ creeping zone except for the clasts of serpentine (Figure 6a), which occur relatively rarely in the damage zone. This is the other main difference with the mineral composition of the rock outside the creeping zone. The amount of serpentine in the creeping zone ranges between 10% and 15%. X-ray diffraction and microprobe analyses indicate two kinds of serpentines, chrysotile and lizardite, which were imaged using a FEG-SEM (Figure 7). Many polymineral clasts are composed of fractured serpentine with calcite veins. Quartz and feldspar are the most common minerals forming the polymineral clasts. Note that most of those polymineral clasts are fractured. Small amounts of chlorite, iron, and titanium oxides as well as very rare talc grains can be found in some aggregates. Most of the polymineral clasts have a

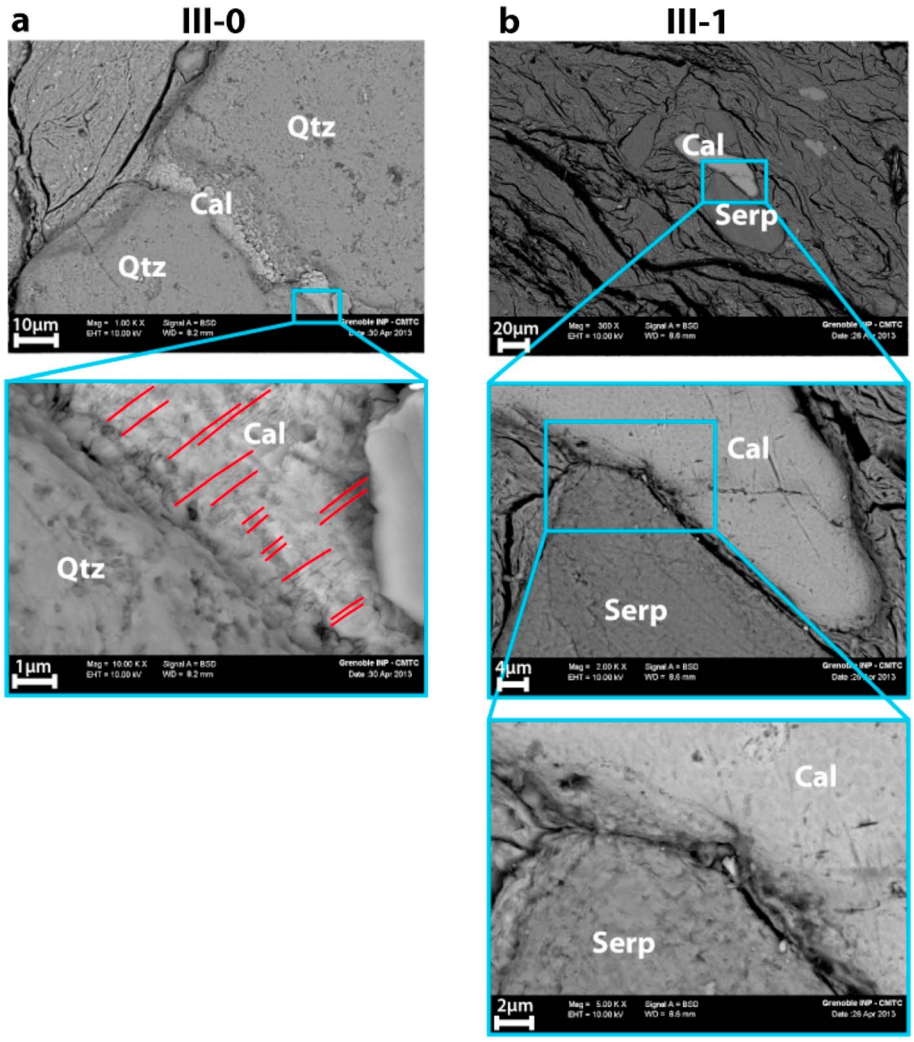

Figure 8. Samples located inside the active creeping zone with grain sliding accommodating the creep: FEG-SEM images showing evidence of a pressure solution process at the grain contacts. (a) Striated calcite between two quartz grains. The quartz grain boundaries are also striated and show evidence of indentations. (b) Contact between a calcite grain and a serpentine grain. The boundaries of the grains are striated and indented, especially in the area of contact.

typical almond shape with parenthesis-shaped pressure dissolution seams (Figure 6c). They are characterized by both concentrations of dark minerals inside the cleavage planes and pressure shadows at the ends of the almond shapes, with calcite growth (Figure 6c). Numerous very small grains ($<10\,\mu m$) were also found to be present, dispersed within the clay matrix (saponite), and usually consisting of serpentine, calcite, quartz, feldspar, and iron oxide. It should also be noted that these grains often had very irregular edges (Figures 6d–6f). Striae are seen on grain-sliding surfaces (Figure 8).

The final notable feature is the very thin shear planes oblique to the foliation in different directions and different scales, observed in all thin sections (Figures 6g and 6h). Highly localized, thin precipitations of hydrous illite-smectite and chlorite-smectite mixed-layered mineral nanocoatings were described by *Schleicher et al*. [2006, 2010], growing preferentially on such polished shear fracture surfaces, with occasional slickensides. Using $^{40}Ar/^{39}Ar$ dating, *Schleicher et al*. [2010] concluded that the hydrous mixed-layered minerals could have first formed during the Pliocene epoch in the CDZ (4 Ma). In some places it is difficult to determine the coherence of all these shear planes and foliation surfaces and to find a main shear sense. As already mentioned by *Janssen et al*. [2012], a significant contrast can be seen between zones with weak clay fabrics and zones with a high degree of preferred alignment of clay particles. Between the different shearing planes, oblique and highly folded foliation can be seen, with also few coherent orientations

(Figure 6). As for the shear planes, the foliation has different scales and various orientations. The rotation of the foliation and the shear planes is mostly correlated to the presence of the polymineral clasts at all scales.

4. Discussion

4.1. The Mechanisms of Deformation and Their Interactions

4.1.1. Fractured and Indented Structures (Relatively Undeformed Zones)

Some specific deformation processes can be found in the relatively undeformed host rocks. The fractured grains may show multiple radial cracks at their contacts (Figures 4a and 4b) that suggest dynamic fracturing processes [*Sagy et al*., 2001]. The damage zone in the vicinity of the SAFOD borehole is seismically active at the present time, with numerous sites of repeating microearthquakes (Figure 2b) from *M*0.1 to *M*3.4, occurring at depths of 2–12 km and with recurrence intervals ranging from 0.6 to 7.1 years [*Nadeau et al*., 2004; *Waldhauser et al*., 2004]. This means that the recent *M*0.1 to *M*3 microearthquakes (and the smaller ones that cannot be detected) must be associated with at least some of the fractures that are seen in the core samples [*Hadizadeh et al*., 2012; *Mittempergher et al*., 2011], corresponding to rupture patches from a few centimeters to a hundred meters in diameter with micron- to centimeter-scale displacements [*Wells and Coppersmith*, 1994]. There is further evidence that the faults appearing in the core have recorded seismic events: observation of injected shale in such faults and observation of large voids opening faster than calcite growth [*Mittempergher et al*., 2011]. Other observations relate these faults to the present-day seismicity: (i) the observation that the surface displacement associated with the last *M*6 Parkfield earthquake propagating up to the SAFOD borehole [*Langbein et al*., 2005]; (ii) the evidence of K-feldspar luminescence resetting, possibly linked to an earthquake, notably one that would have occurred 139 ± 12 years before 2010, possibly corresponding to the effect of the 1857 Fort Tejon earthquake [*Spencer et al*., 2012].

Multiple grain indentations give evidence of pressure solution deformation (Figures 4d and 4e), a mechanism that requires certain specific conditions in order to occur [*Paterson*, 1973; *Rutter*, 1976; *Weyl*, 1959]. Pressure solution is activated by the presence of fluids that must dissolve at least one of the minerals contained in the rock. It is also enhanced by fracturing or by comminution processes, because the strain rate in pressure solution creep laws is inversely proportional to the distance of mass transfer d when the strain rate is controlled by diffusion [*Raj*, 1982; *Rutter*, 1983; *Weyl*, 1959]. This is demonstrated by dynamic pressure solution indenting that shows that the dissolution is drastically accelerated by fracturing [*Gratier et al*., 1999, 2014]. Clear interactions are therefore observed between fracturing and pressure solution (Figures 4d and 4e). Interaction between pressure solution and faults can also be observed as faults are found to be zones of dissolution and passive concentration of phyllosilicates [*Hadizadeh et al*., 2012, Figure 3]. Given that pressure solution is a very slow process (strain rate lower than $10^{-10}\,s^{-1}$), then at least part of the displacement along the fault occurs at very slow displacement rate, possibly during postseismic shear deformation in a volume around the seismic slip surface. This zone illustrates a type of deformation behavior with mainly brittle deformation by earthquakes followed by a small amount of postseismic deformation that occurs not only along the fault (afterslip with dissolution along the fault) but also in the vicinity of the seismic zone. Intense fracturing facilitates pressure solution indenting by reducing the mass transfer distance d, then healing and sealing slow down the creep by increasing d, thus strengthening the rocks. Hence, stress could buildup, leading to new brittle deformation that would accelerate the rate of pressure solution creep and repeat the deformation as a cycle [*Gratier et al*., 1999].

4.1.2. Fractured and Foliated Shear Zones

Tectonic layering, associated with pervasive foliation, leads to localized deformation with two end-member zones with different rheologies: the dissolution zone and the deposition zone. The development of a dissolution zone with no or little deposition (i.e., an open system allowing the depletion of soluble species) as described in some places, facilitates and consequently localizes the deformation. This is because, with all conditions being the same, a mixture of insoluble and soluble species deforms more easily by pressure solution than a monomineralic rock composed of only soluble species. This can be explained by the fact that the kinetics of diffusive mass transfer along phyllosilicate/soluble mineral boundaries is much faster than along the boundaries of soluble minerals that can heal. This is demonstrated by natural observation [*Gratier*, 2011] and by experiments [*Niemeijer and Spiers*, 2005; *Zubtsov et al*., 2004]. In the dissolution zone, the passive concentration of insoluble species, such as phyllosilicates, activates the kinetics of mass transfer. This leads to a positive feedback process that facilitates the localization of dissolution. Moreover, weakening is

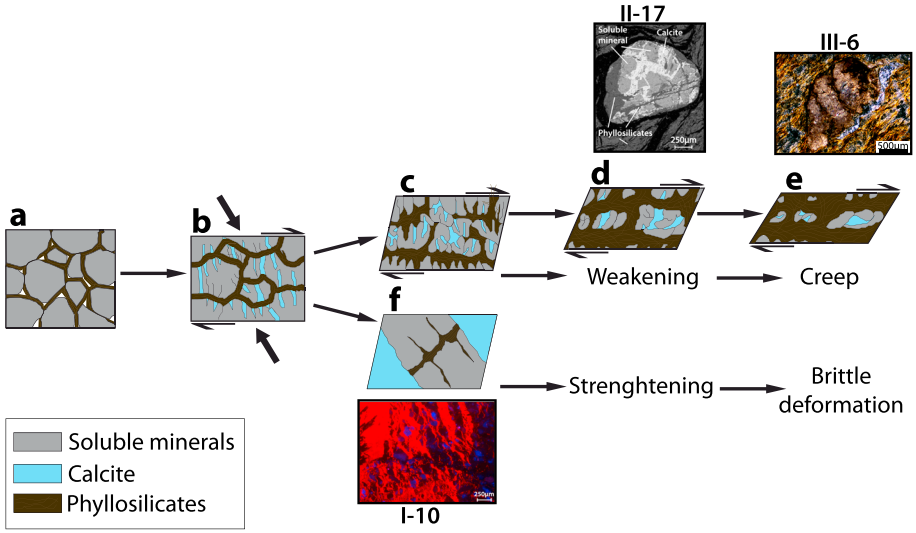

Figure 9. Model of mineral change inside the damaged zone. (a) Initial state: the grey grains are soluble minerals such as quartz, feldspars, and serpentine. (b) Deformation starts with compression and shearing, which leads to fracturing at indenting contacts and activation of pressure solution creep. Soluble minerals start dissolving, calcite (in blue) is precipitated into the fractures and phyllosilicates (in brown) begin to be passively concentrated. (c) A foliation is developed with the passive concentration of phyllosilicates. The opening of veins becomes wider. (d) With time, the soluble minerals continue to dissolve. Because of fluid circulation, the main part of the dissolved material is transported away. Phyllosilicate concentration increases with the growth and crystallization of clay. Polymineral clasts start to be formed and act as hard objects. (e) Final state: rotation of the hard objects. Initially, they were the aggregates protected by the calcite or the monomineralic aggregates, harder to dissolve. (f) Alternatively, the large calcite veins wedge the system and stop the ductile deformation.

linked both to mechanical and chemical processes: decrease in friction and activation of dissolution, respectively, due to phyllosilicate concentration (Figure 9). This decrease in friction due to an increase in phyllosilicate content is demonstrated by experiments: the friction along phyllosilicates is easier than along other minerals (quartz and feldspars even halite) and the pressure solution process is activated by the presence of the phyllosilicates [*Bos and Spiers*, 2002; *Bos et al*., 2000]. The mass transfer mechanism associated with this depletion of the soluble species imposes the size of the localized zone: decimeter scale if controlled by diffusion and hectokilometer scale if controlled by fluid advection [*Cox and Etheridge*, 1989; *Gratier and Gueydan*, 2007].

Conversely, in the deposition zone the presence of a large amount of calcite-filled veins tends to strengthen the rocks as it is more difficult to dissolve monomineralic rocks than a mixture of soluble and insoluble grains [*Gratier et al*., 2013b]. Dissolution is not observed at grain scale in the veins but only at the boundary of such veins (Figure 5), where the thin fluid phase is located. Since, for an imposed strain rate, pressure solution creep is more difficult in such zones, this leads to a positive feedback loop: the strengthening leads to fractures that become sealed and the zones become increasingly stronger, localizing the fracturing processes (Figure 9). Inside the sealed calcite veins, the different red colors of calcite displayed in cathodoluminescence indicate that several sealing episodes were probably connected to successive fluid flow episodes [*Mittempergher et al*., 2011].

The observation of cleavage seams of various orientations (Figure 5) indicates that they develop in a shear zone, but as the cores are not oriented, it is difficult to evaluate the sense of such a shear zone relative to the kinematics of the SAF. However, palinspastic reconstructions [*Powell*, 1993] show that the plate boundary has undergone complex changes over the past 20 Myr, affecting a large zone several kilometers wide with continental block rotations [*Nicholson et al*., 1994]. The SAF fault zone was certainly affected by the regional deformation; however, it is likely that most of the deformation structures within the laterally continuous and localized modern fault zone (200 m) are related to the recent motion of the fault (5 Myr) because regional structures related to subduction have a totally different orientation and intensity than the ones related to the SAF right lateral movement: sparse anastomosing cleavage for the regional part and dense vertical cleavage for the localized fault zone. The observation of dissolution of both quartz and calcite, which have

opposite solubility change with temperature, with associated calcite precipitation, indicates that deformation occurs at relatively low temperature 150–250°C [*Gratier et al*., 2013a]. Regardless of the age of this deformation, it had a significant effect in transforming the rocks.

Our observations support the idea of multiple deformation episodes, combining creep, fracturing, sealing, and fluid flow through the damage zone associated with the SAF right lateral movement. This may be indicative of "mixed mode" seismicity as suggested by *Faulkner et al*. [2003] and *Collettini et al*. [2011] with fault creep within the phyllosilicate-rich fault gouge layers (the shear zone weakened by dissolution), punctuated by larger events nucleating within the zone that have been strengthened by calcite precipitation. While it is difficult to evaluate the relative role of each mechanism, the strain values associated with solution cleavage in the shear zones (shortening: $l_s/l_0 < 0.4$) could not, however, have accommodated shear strain values of more than 2 (see section 3.2.2). With such strain values, solution cleavage would accommodate only a small part of the total shear strain value that is required by the offset of the San Andreas Fault (90 km since the Pliocene [*Weldon et al*., 1993]). Consequently, as solution cleavage is observed to be closely related to fracturing, this creeping mechanism may have been mainly a postseismic process. At that time, the shear zones were not soft enough to accommodate steady state creeping. Another weakening process was needed that is discussed below.

4.1.3. Grain Sliding Accommodating Active Creep

A specific feature of the CDZ main active creeping zone is that it is the only part in the SAF that contains more than 50% of soft phyllosilicates as saponite (Figure 6). Laboratory experiments have underlined the importance of gouge mineralogy on the fault zone frictional properties [*Carpenter et al*., 2009; *Ikari et al*., 2009, 2011] and especially for the phyllosilicate-rich fault gouges [*Niemeijer and Spiers*, 2006; *Vrolijk and van der Pluijm*, 1999]. The average friction coefficient of the CDZ determined by laboratory friction experiments is in the range 0.16–0.21 [*Carpenter et al*., 2011; *Lockner et al*., 2011]. In the case of a montmorillonite/quartz mixture, *Tembe et al*. [2010] showed that the clay content must be greater than 50% to reach a friction coefficient lower than 0.2. Experimental studies on rock with a fabric of interconnected network of phyllosilicates in wet conditions have shown that a smaller amount of phyllosilicates can result in low friction [*Collettini et al*., 2009a; *Niemeijer et al*., 2010]. Such results, indicating that a quite large quantity of weak grains in a gouge is necessary to reduce significantly the overall friction, have also been simulated using a discrete element method [*Rathbun et al*., 2013]. Therefore, the most important parameter to activate the low friction creep mechanism is the mineral composition of the fault core: there should be a sufficiently high concentration of low friction minerals.

In the CDZ, the specific structure is associated with both sliding on clay minerals along numerous microshearing planes and rotation of the polymineral clasts (Figure 6). According to *Janssen et al*. [2012], weak fabrics in intensely strained ultracataclasite fault gouges are attributed to (i) newly formed clay minerals that grew in many orientations, (ii) folded and kinked clay minerals, and (iii) clay particles wrapped around grains. The sliding of clay minerals may be associated with the development of microshearing planes and the rotation of polymineralic clasts and smaller grains (Figure 10b). The rotation of all these rigid objects drags the foliation and contributes to the chaotic microstructure observed in the CDZ (Figure 10c). Alternatively, if the clasts cannot rotate between two shear planes, the system is locked, and the only way to continue deforming is to develop constantly new foliations, superimposed on the previous ones (Figure 10d) or to fracture the clast. The possible rotation of the polymineral clasts may be linked to their shape ratio and to their interaction with the matrix. Indenting by pressure solution at the boundary of such polymineral clasts suggests that pressure solution contributes to the general grain-clast boundary sliding of all the minerals of the creeping zone. Such an interpretation is compatible with the frictional-viscous flow of the phyllosilicate-bearing rock model proposed by *Bos and Spiers* [2002], *Bos et al*. [2000], and *Jefferies et al*. [2006] that couples frictional and diffusional grain-sliding deformation. Grain sliding is the only process that can accommodate the almost infinite shear values [*Ashby and Verall*, 1973] that are required in steady state creeping zones.

The observations of fractured serpentine clasts with calcite veins rule out the common statement that serpentine is always a soft mineral. Serpentine minerals may have varied behavior. Most often, when sealed together in clasts, they behave as rigid bodies that can acquire a brittle behavior with only dissolution at their boundary. Like quartz, feldspar, and calcite, pressure solution of serpentine minerals is more efficient when they are mixed with other minerals (see section 4.1.2).

This CDZ zone with grain sliding accommodating active creep illustrates a steady state ductile behavior that should have developed progressively thanks to two associated mechanisms: the passive concentration of

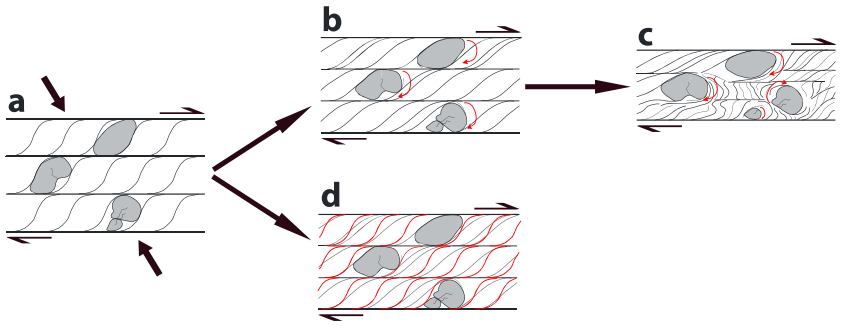

Figure 10. Model of clay deformation leading to foliation without preferential orientation. (a) Initial state, with a normal foliation oriented at about 45° to the shear plane. (b) The foliation follows a normal trend, tending to become parallel with the shear planes. But the presence of hard objects (aggregates and grains of all sizes) hinders this parallelization and stops the development of the foliation. (c) The grains start to rotate, continuing to accommodate the deformation. This rotation is controlled by the sliding of the clay minerals one against the other or by pressure solution creep at grain boundaries, when soluble grains are in contact or under stress. (d) If the grains do not rotate, the system is locked. To continue deformation, the only way is to develop a new foliation, superimposed on the previous one. This process can be repeated every time the grains lock the system.

phyllosilicates due to pressure solution and the metamorphic transformation of the phyllosilicates to saponite (Mg-rich smectite). The mineral composition has changed because of growth and/or precipitation of new minerals by metasomatic reactions. For example, saponite is the product of the reaction between the deformed rocks and external fluids [*Lockner et al*., 2011; *Moore and Rymer*, 2012]. Such an assumption relies on fluid flow through the creeping zone, possibly episodic and related to earthquakes, that evacuates certain elements (Si, Na, Ca, …) and brings in others (Mg). The dating of the neocrystallized clay coating thin film by *Schleicher et al*. [2010] indicates that such transformations occurred relatively recently (0–8 Myr).
The chronology of this change is discussed below.

4.2. From the Fractured and Foliated Shear Zones to the Active Creeping Zone: Development in Time and Space

4.2.1. Creep Mechanism Development With Time

The observations and interpretations made in this study document the time-dependent change in the mineral composition and the spatial transformation of the microstructures from fractured and foliated zones to actively creeping zones. This chronology is deduced from various observations. Clasts of the foliated zones are included in the present-day creeping zone (Figure 6). They show solution cleavage and associated vein structures that have been rotated during the active creeping process (Figures 9 and 10) reflecting the early development of such structures (see section 3.2.3). This is good evidence that at the beginning of the process, the entire damage zone was creeping mostly by pressure solution cleavage (Figures 11 and 12), associated with episodic earthquakes. Solution cleavage was initiated at grain indentation and became pervasive in the shear zones. The development of such deformation indicates that the CDZ was not as soft as it is today.

Interactions between fracturing, sealing, and pressure solution in the damage zone led to localized deformation processes. In the initially stronger rock, fracturing and subsequent efficient sealing strengthened the rocks: the stronger the rock, the more likely it may break and be sealed by new calcite that renders the rock even stronger (Figure 9). Conversely, in the zone with minimum deposition and maximum fluid flow, rocks were softened progressively thanks to the effect of the progressive concentration of phyllosilicates. Moreover, phyllosilicates growth have been found localized preferentially along preexisting ultracataclasite zones since these were finer grained and potentially more permeable [*Imber et al*., 2001; *Jefferies et al*., 2006; *Stewart et al*., 2000]. This could also contribute to the localization of the phyllosilicates. Such a change has been observed in other faults [*Collettini et al*., 2011; *Faulkner et al*., 2003; *Gratier et al*., 2013b]. This progressive weakening may initially have been induced by the occurrence of successive earthquakes (Figure 11) that could have contributed to opening the system, promoting episodic fluid flow [*Mittempergher et al*., 2011], reducing the grain size [*Gratier et al*., 2011, Figure 2] and promoting pressure solution with two types of deformation [*Gratier et al*., 2013b]: in some parts, deposition associated with dissolution strengthens the rocks (this corresponds to the present-day damage zone, Figure 11, bottom part),

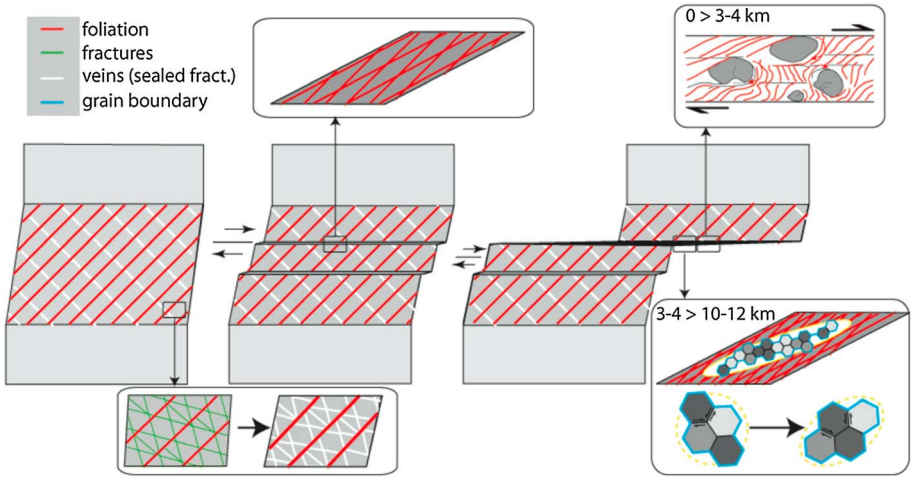

Figure 11. Schematic model of the change in a creeping zone. On the left, a creeping zone, up to several hundred meters wide, initiates in a zone combining several conditions favorable to pressure solution creep: (i) presence of fluids that can dissolve at least part of the rock, (ii) mixture of soluble and insoluble minerals, (iii) small grain size or fractured grains. The creeping rate is not large enough to relax the stress so earthquakes occur through this zone (middle part). This has two effects: grain size reduction, which activates pressure solution creep, and fluid flow enhancement through the precreeping zone. These fluids evacuate the soluble species and thus concentrate phyllosilicates, also promoting pressure solution creep. On the right-hand side, a meter-wide creeping zone is stable: in the top part of the crust (0 to 3–4 km) creep is promoted both by the very low friction of the clay minerals (saponite) that derived from both the passive concentration of phyllosilicate and the metamorphic reactions linked to episodic fluid flows. In the bottom part of the crust (3–4 to 10–12 km), diffusion-accommodated grain-sliding pressure solution creep is efficient enough to accommodate aseismic sliding.

whereas in other parts departure of the mobile species weakens the rock (this corresponds to the present-day active creeping zone, Figure 11, top part). The end-member of such a transformation is a zone without any soluble species in which the friction of the phyllosilicates controls the shear strength (Figure 11, top part).

The composition of the CDZ was slightly different from the surrounding rocks with higher initial content in Mg with both serpentines and Mg-rich chlorites in the protocreeping zone. Its main transformation resulted from both passive concentration of such Mg-rich phyllosilicates (Figure 9) and from metasomatic reactions associated with successive fluid flow and leading to saponite (see section 4.1.2). The presence of polymineralic clasts with cleavage/vein deformation documents the temporal transformation of the rocks from fractured and foliated shear zones to active creeping zones (Figures 11 and 12). The deformation evolved from a zone with earthquake and postseismic creep (fracturing and foliated zone) to a zone of steady state creep (grain sliding accommodating active creep zone) (Figure 11, right part).

4.2.2. Change in Creeping Mechanisms With Depth

The change in creep mechanisms with depth is strongly dependent on rock composition and microstructure. Figure 12 shows the change in mineralogy as a function of time, depth, and creeping zone distance. Within the blue domain corresponding to the damaged zone, pressure solution creep is the main creep mechanism. Healing by calcite precipitation progressively strengthens this domain. The red domain corresponds to the active creeping zone: pressure solution creep is very efficient at the beginning at all depths. However, departure of the mobile species washed away by episodic fluid flow leads to increasing clay content by both the passive concentration of phyllosilicates and their metamorphic transformation into soft minerals such as saponite. This weakens this domain with two types of creep mechanisms depending on the depth (Figure 12, right part). As the temperature increases with depth, mineral composition changes leading to dissolution-precipitation reactions [*Putnis*, 2002; *Wintsch and Yi*, 2002]. In the San Andreas Fault, saponite clay, which is a stable mineral up to about 110°C, will transform at depth into corrensite, which is stable up to 150°C and is likely to change into Mg-rich chlorite at greater depth [*Moore and Rymer*, 2012]. Those mineral transformations tend to strengthen the creeping zone at depth. The friction coefficients of phyllosilicates such as illite (0.25–0.4) and chlorite (0.26–0.38) at depth [*Brown et al.*, 2003; *Ikari et al.*, 2009] are higher than that of saponite (0.2). With such values of friction [*Schleicher et al.*, 2012] and some level of fluid overpressure (that has not been seen in the SAFOD hole), the fault could slip by frictional sliding along phyllosilicates without too much frictional heating. It remains that the accommodation of deformation by low-friction saponite is efficient near the surface

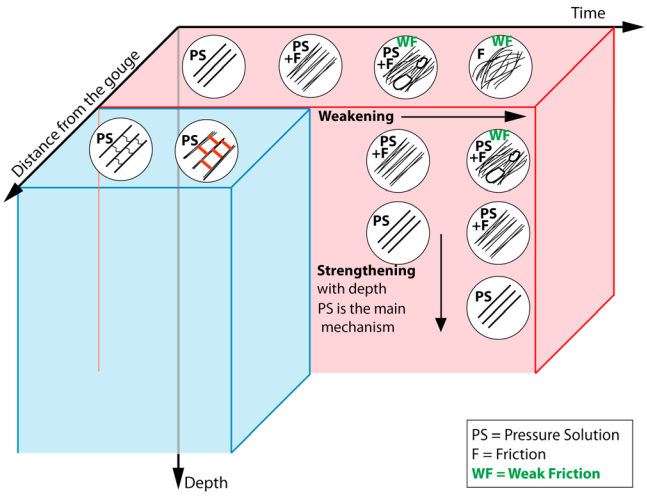

Figure 12. Model of a creeping fault zone showing the change in mineralogy as a function of time, depth, and creeping zone distance. The blue domain corresponds to the creep mechanism observed in the damaged zone, in the samples outside the creeping zone. In this domain, pressure solution creep is the main creep mechanism. Healing by calcite precipitation allows this mechanism to be maintained with time as well as at depth. The red domain corresponds to the creep mechanisms observed in the active creeping zone. Pressure solution creep is very efficient at the beginning at all depths. However, because there is no or little healing in this domain because fluids drive away the dissolved materials, the mineralogical composition evolves with time, leading to increasing clay content in the upper 3–4 km. The friction coefficient of the creeping domain becomes very low, and the sliding of clay layers on top of each other could accommodate a substantial part of the creeping rate. It is completed by stress-driven diffusive mass transfer that accommodates the sliding of grains and clast aggregates. Low friction related to saponite is not operative below 3–4 km because of the transformation of saponite into corrensite then chlorite, which have higher friction coefficients. When saponite starts to transform into harder minerals with the increase in temperature, the entire domain becomes stronger and more difficult to deform by friction. Diffusion-accommodated grain-sliding pressure solution creep remains efficient and is the main creep mechanism at depth.

(up to 3–4 km of depth [*Carpenter et al.*, 2011; *Lockner et al.*, 2011]) but becomes less efficient and more energy consuming with depth (Figure 12). On the other hand, the required conditions for efficient pressure solution creep are fulfilled if a trapped fluid phase is kept within the creeping zone and if fracturing and comminution processes have reduced the grain size, i.e., the characteristic mass transfer distance. In such a case, diffusive grain boundary sliding controlled by pressure solution is likely to be the most efficient process at depth. Such a process is comparable to superplasticity [*Ashby and Verall*, 1973]. Only the diffusive path is different: in natural deformation diffusion-accommodated grain sliding can occur along dry grain boundaries at relatively high temperature [*Boullier and Guéguen*, 1975]. Alternatively, it is proposed that such a diffusion-accommodated grain-sliding process could occur by pressure solution with diffusion along the trapped fluid phase consequently at much lower temperature [*Gratier et al.*, 2011]. Such a process is able to accommodate almost infinite shear deformation (Figure 12).

5. Conclusion

From microstructural observations of rock samples collected at depth in the active creeping zone of the San Andreas Fault and its surrounding damage zone, it is suggested that interactions between brittle and viscous mechanisms led to widespread transformation of the rocks and that the shear zone representing the plate boundary has evolved from a zone with earthquakes and postseismic creep to a zone of steady state creep.

In a first stage, the deformation zone was probably wide, corresponding approximately to the damaged zone associating earthquakes and postseismic creep. Postseismic creep was mostly controlled by pressure solution creep. Interactions between fracturing, sealing, and mass transfer led to rock differentiation with two end-members: (a) in zones where fractures were sealed, the pressure solution creep rate was slower because sealing decreased the efficiency of diffusive mass transfer and the rocks were strengthened and increasingly fractured; (b) in zones of dissolution of soluble minerals (quartz, feldspars, calcite, and serpentines) washed away by episodic fluid flow, the passive concentration of phyllosilicates increased the rate of pressure solution and consequently weakened such zones. Some of these weakened zones with specific mineral composition were weakened even further by the metamorphic transformation of phyllosilicates into soft clays in the form of saponite. These zones concentrate all the creep displacement with mainly low-friction grain sliding coupled with local diffusive grain sliding.

Within the first 3–4 km depth, the deformation in the active creeping zone is controlled by the very low friction of saponite and diffusive grain sliding. At greater depths (4–12 km), saponite is transformed into corrensite and then into chlorite, both with higher friction coefficients. Hence, pressure solution diffusive grain boundary sliding is likely to be the controlling creeping mechanism if soft minerals are not present.

Acknowledgments
We thank B. Holdsworth and an anonymous reviewer for their suggestions and their comments that significantly improved the manuscript. The data on the thin sections are available from ICDP web site (http://www-icdp.icdp-online.org/front_content.php?idcat=896). This project was funded by a grant from the University Joseph Fourier and by the LABEX OSUG@2020 (Investissement d'avenir-ANR10-LABX56).

References

Allen, C. R. (1968), The tectonic environments of seismically active and inactive areas along the San Andreas fault system, in *Geologic Problems of San Andreas Fault System*, *Pubs. Geol. Sci., vol.* 11, edited by W. R. Dickinson and A. Grantz, pp. 70–82, Stanford Univ., Stanford, Calif.

Andreani, M., A.-M. Boullier, and J.-P. Gratier (2005), Development of schistosity by dissolution crystallization in a Californian serpentinite gouge, *J. Struct. Geol.*, *27*, 2256–2267.

Ashby, M., and R. Verall (1973), Diffusion-accommodated flow and superplasticity, *Acta Metall.*, *21*, 149–163.

Azzaro, R., M. Mattia, and G. Puglisi (2001), Fault creep and kinematics of the eastern segment of the Pernicana Fault (Mt. Etna, Italy) derived from geodetic observations and their tectonic significance, *Tectonophysics*, *333*, 401–415.

Bakun, W. H., and T. V. McEvilly (1984), Recurrence models and Parkfield, California, earthquakes, *J. Geophys. Res.*, *89*, 3051–3058, doi:10.1029/JB089iB05p03051.

Barbot, S., Y. Fialko, and Y. Bock (2009), Postseismic deformation due to the M_w 6.0 2004 Parkfield earthquake: Stress-driven creep on a fault with spatially variable rate-and-state friction parameters, *J. Geophys. Res.*, *114*, B07405, doi:10.1029/2008JB005748.

Boness, N. L., and M. D. Zoback (2004), Stress-induced seismic velocity anisotropy and physical properties in the SAFOD Pilot Hole in Parkfield, Calif., *Geophys. Res. Lett.*, *31*, L15S17, doi:10.1029/2003GL019020.

Bons, P. D. (2001), Development of crystal morphology during unitaxial growth in a progressively widening vein: I. The numerical model, *J. Struct. Geol.*, *23*, 865–872.

Bos, B., and C. J. Spiers (2002), Frictional-viscous flow of phyllosilicate-bearing fault rock: Microphysical model and implications for crustal strength profiles, *J. Geophys. Res.*, *107*(B2), 2028, doi:10.1029/2001JB000301.

Bos, B., C. J. Peach, and C. J. Spiers (2000), Frictional-viscous flow of simulated fault gouge caused by the combined effects of phyllosilicates and pressure solution, *Tectonophysics*, *327*, 173–194.

Boullier, A.-M., and Y. Guéguen (1975), SP-mylonites: Origin of some mylonites by superplastic flow, *Contrib. Mineral. Petrol.*, *50*, 93–104.

Bradbury, K. K., D. C. Barton, J. G. Solum, S. D. Draper, and J. P. Evans (2007), Mineralogic and textural analyses of drill cuttings from the San Andreas Fault Observatory at Depth (SAFOD) boreholes: Initial interpretations of fault zone composition and constraints on geologic models, *Geosphere*, *3*, 299–318.

Brantley, S., B. Evans, S. Hickman, and D. A. Crerar (1990), Healing of microcracks in quartz: Implications for fluid flow, *Geology*, *18*, 136–139.

Brown, K. M., A. Kopf, M. B. Underwood, and J. L. Weinberger (2003), Compositional and fluid pressure controls on the state of stress on the Nankai subduction thrust: A weak plate boundary, *Earth Planet. Sci. Lett.*, *214*, 589–603.

Brune, J. N., T. L. Henyey, and R. F. Roy (1969), Heat flow, stress, and rate of slip along the San Andreas Fault, California, *J. Geophys. Res.*, *74*, 3821–3827, doi:10.1029/JB074i015p03821.

Burford, R. O., and P. W. Harsh (1980), Slip on the San Andreas Fault in Central California from alignment array surveys, *Bull. Seismol. Soc. Am.*, *70*, 1233–1261.

Byerlee, J. (1978), Friction of rocks, *Pure Appl. Geophys.*, *116*, 615–626.

Carpenter, B. M., C. Marone, and D. M. Saffer (2009), Frictional behavior of materials in the 3D SAFOD volume, *Geophys. Res. Lett.*, *36*, L05302, doi:10.1029/2008GL036660.

Carpenter, B. M., C. Marone, and D. M. Saffer (2011), Weakness of the San Andreas Fault revealed by samples from the active fault zone, *Nat. Geosci.*, *4*, 251–254.

Chéry, J., M. D. Zoback, and S. Hickman (2004), A mechanical model of the San Andreas fault and SAFOD Pilot Hole stress measurements, *Geophys. Res. Lett.*, *31*, L15S13, doi:10.1029/2004GL019521.

Chester, F. M., J. P. Evans, and R. L. Biegel (1993), Internal structure and weakening mechanisms of the San Andreas Fault, *J. Geophys. Res.*, *98*, 771–786, doi:10.1029/92JB01866.

Collettini, C., A. Niemeijer, C. Viti, and C. J. Marone (2009a), Fault zone fabric and fault weakness, *Nature*, *462*, 907–910, doi:10.1038/nature08585.

Collettini, C., C. Viti, S. A. F. Smith, and R. E. Holdsworth (2009b), Development of interconnected talc networks and weakening of continental low-angle normal faults, *Geology*, *37*, 567–570.

Collettini, C., A. Niemeijer, C. Viti, S. A. F. Smith, and C. Marone (2011), Fault structure, frictional properties and mixed-mode fault slip behavior, *Earth Planet. Sci. Lett.*, *311*(3–4), 316–327, doi:10.1016/j.epsl.2011.09.020.

Cox, S. F., and M. A. Etheridge (1989), Coupled grain-scale dilatancy and mass transfer during deformation at high fluid pressures: Examples from Mount Lyell, Tasmania, *J. Struct. Geol.*, *11*, 147–162.

d'Alessio, M. A., C. F. Williams, and R. Bürgmann (2006), Frictional strength heterogeneity and surface heat flow: Implications for the strength of the creeping San Andreas fault, *J. Geophys. Res.*, *111*, B05410, doi:10.1029/2005JB003780.

Draper-Springer, S., J. P. Evans, J. I. Garver, D. Kirschner, and S. U. Janecke (2009), Arkosic rocks from the San Andreas Fault Observatory at Depth (SAFOD) borehole, Central California: Implications for the structure and tectonics of the San Andreas fault zone, *Lithosphere*, *1*, 206–226.

Ellsworth, W. L. (1990), Earthquake history, 1769–1989, in *The San Andreas Fault System, California*, edited by R. E. Wallace, *U.S. Geol. Surv. Prof. Pap.*, *1515*, 283.

Etheridge, M. A., S. F. Cox, V. J. Wall, and R. H. Vernon (1984), High fluid pressures during regional metamorphism and deformation: Implications for mass-transport and deformation mechanisms, *J. Geophys. Res.*, *89*, 4344–4358, doi:10.1029/JB089iB06p04344.

Faulkner, D. R., A. C. Lewis, and E. H. Rutter (2003), On the internal structure and mechanics of large strike-slip fault zones: Field observations of the Carboneras fault in southeastern Spain, *Tectonophysics*, *367*, 235–251.

Freed, A. M. (2007), Afterslip (and only afterslip) following the 2004 Parkfield, California, earthquake, *Geophys. Res. Lett.*, *34*, L06312, doi:10.1029/2006GL029155.

Fulton, P. M., and D. M. Saffer (2009), Potential role of mantle-derived fluids in weakening the San Andreas Fault, *J. Geophys. Res.*, *114*, B07408, doi:10.1029/2008JB006087.

Fulton, P. M., D. M. Saffer, R. N. Harris, and B. A. Bekins (2004), Re-evaluation of heat flow data near Parkfield, CA: Evidence for a weak San Andreas Fault, *Geophys. Res. Lett.*, *31*, L15S15, doi:10.1029/2003GL019378.

Fulton, P. M., D. M. Saffer, and B. A. Bekins (2009), A critical evaluation of crustal dehydration as the cause of an overpressured and weak San Andreas Fault, *Earth Planet. Sci. Lett.*, *284*, 447–454.

Gao, S. S., P. G. Silver, and A. T. Linde (2000), Analysis of deformation data at Parkfield, California: Detection of a long-term strain transient, *J. Geophys. Res.*, *105*, 2955–2967, doi:10.1029/1999JB900383.

Gratier, J.-P. (2011), Fault permeability and strength evolution related to fracturing and healing episodic processes (years to millennia): The role of pressure solution, *Oil Gas Sci. Technol.*, *3*, 491–506.

Gratier, J.-P., and F. Gueydan (2007), Deformation in the presence of fluids and mineral reactions: Effect of fracturing and fluid-rocks interaction on seismic cycle, in *Tectonic Faults, Agent of Change on a Dynamic Earth*, Dahlem Workshop, edited by M. R. Handy, G. Hirth, and N. Hovius, pp. 319–356, MIT Press, Cambridge, Mass.

Gratier, J.-P., F. Renard, and P. Labaume (1999), How pressure solution creep and fracturing processes interact in the upper crust to make it behave in both a brittle and viscous manner, *J. Struct. Geol.*, *21*, 1189–1197.

Gratier, J.-P., J. Richard, F. Renard, S. Mittempergher, M. L. Doan, G. Di Toro, J. Hadizadeh, and A.-M. Boullier (2011), Aseismic sliding of active faults by pressure solution creep: Evidence from the San Andreas Fault Observatory at Depth, *Geology*, *39*(12), 1131–1134.

Gratier, J.-P., D. K. Dysthe, and F. Renard (2013a), The role of pressure solution creep in the ductility of the Earth's upper crust, *Adv. Geophys.*, *54*, 47–179.

Gratier, J.-P., F. Thouvenot, L. Jenatton, A. Tourette, M. L. Doan, and F. Renard (2013b), Geological control of the partitioning between seismic and aseismic sliding behaviours in active faults: Evidence from the Western Alps, France, *Tectonophysics*, *600*, 226–242.

Gratier, J.-P., F. Renard, and B. Vial (2014), Postseismic pressure solution creep: Evidence and time-dependent change from dynamic indenting experiments, *J. Geophys. Res. Solid Earth*, *119*, 2764–2779, doi:10.1002/2013JB010768.

Hadizadeh, J., S. Mittempergher, J.-P. Gratier, F. Renard, G. Di Toro, J. Richard, and H. Babaie (2012), A microstructural study of fault rocks from the SAFOD: Implications for the deformation mechanisms and strength of the creeping segment of the San Andreas Fault, *J. Struct. Geol.*, *42*, 246–260.

Handy, M. R. (1990), The solid state flow of polymineralic rocks, *J. Geophys. Res.*, *96*, 8647–8661, doi:10.1029/JB095iB06p08647.

Hanks, T. C., and C. B. Raleigh (1980), The conference on magnitude of deviatoric stresses in the Earth's crust and uppermost mantle, *J. Geophys. Res.*, *85*, 6083–6085, doi:10.1029/JB085iB11p06083.

Hickman, S., and M. D. Zoback (2004), Stress orientations and magnitudes in the SAFOD pilot hole, *Geophys. Res. Lett.*, *31*, L15S12, doi:10.1029/2004GL020043.

Hickman, S., M. D. Zoback, W. Ellsworth, N. Boness, P. Malin, S. Roecker, and C. Thurber (2007), Structure and properties of the San Andreas Fault in Central California: Recent results from the SAFOD experiment, *Sci. Drill.*, *1*, 29–32.

Hobbs, B. E., W. D. Means, and P. F. Williams (1976), *An Outline of Structural Geology*, 571 pp., Wiley, New York.

Holdsworth, R. E., E. Tavarnelli, P. Clegg, R. V. L. Pinheiro, R. R. Jones, and K. J. W. McCaffrey (2002), Domainal deformation patterns and strain partitioning during transpression: An example from the Southern Uplands terrane, *Scotland J. Geol. Soc.*, *159*, 401–415, doi:10.1144/0016-764901-123.

Holdsworth, R. E., E. W. E. van Diggelen, C. J. Spiers, J. H. P. de Bresser, R. J. Walker, and L. Bowen (2011), Fault rocks from the SAFOD core samples: Implications for weakening at shallow depths along the San Andreas Fault, California, *J. Struct. Geol.*, *33*, 132–144, doi:10.1016/j.jsg.2010.11.010.

Ikari, M. J., D. M. Saffer, and C. Marone (2009), Frictional and hydrologic properties of clay-rich fault gouge, *J. Geophys. Res.*, *114*, B05409, doi:10.1029/2008JB006089.

Ikari, M. J., C. Marone, and D. M. Saffer (2011), On the relation between fault strength and frictional stability, *Geology*, *39*, 83–86.

Imber, J., R. E. Holdsworth, C. A. Butler, and R. A. Strachan (2001), A reappraisal of the Sibson-Scholz fault zone model: The nature of the frictional to viscous ("brittle-ductile") transition along a long-lived, crustal-scale fault, Outer Hebrides, Scotland, *Tectonics*, *20*(5), 601–624, doi:10.1029/2000TC001250.

Irwin, P. W., and I. Barnes (1975), Effect of geologic structure and metamorphic fluids on seismic behavior of the San Andreas fault system in central and northern California, *Geology*, *3*, 713–716.

Jackson, D. D., and Y. Y. Kagan (2006), The 2004 Parkfield earthquake, the 1985 prediction and characteristic earthquakes: Lessons for the future, *Bull. Seismol. Soc. Am.*, *96*, 397–409, doi:10.1785/0120050821.

Janssen, C., R. Wirth, E. Rybacki, R. Naumann, H. Kemnitz, H. R. Wenk, and G. Dresen (2010), Amorphous material in SAFOD core samples (San Andreas Fault): Evidence for crush-origin pseudotachylytes?, *Geophys. Res. Lett.*, *37*, L01303, doi:10.1029/2009GL040993.

Janssen, C., W. Kanitpanyacharoen, H. R. Wenk, R. Wirth, L. Morales, E. Rybacki, M. Kienast, and G. Dresen (2012), Clay fabrics in SAFOD core samples, *J. Struct. Geol.*, *43*, 118–127.

Jefferies, S. P., R. E. Holdsworth, T. Shimamoto, H. Takagi, G. E. Lloyd, and C. J. Spiers (2006), Origin and mechanical significance of foliated cataclastic rocks in the cores of crustal-scale faults: Examples from the Median Tectonic Line, Japan, *J. Geophys. Res.*, *111*, B12303, doi:10.1029/2005JB004205.

Jeppson, T. N., K. K. Bradbury, and J. P. Evans (2010), Geophysical properties within the San Andreas Fault Zone at the San Andreas Fault Observatory at Depth and their relationships to rock properties and fault zone structure, *J. Geophys. Res.*, *115*, B12423, doi:10.1029/2010JB007563.

Johanson, I. A., E. J. Fielding, F. Rolandone, and R. Bürgmann (2006), Coseismic and postseismic slip of the 2004 Parkfield earthquake from space-geodetic data, *Bull. Seismol. Soc. Am.*, *96*, 269–282, doi:10.1785/0120050818.

Lachenbruch, A. H., and J. H. Sass (1980), Heat flow and energetics of the San Andreas Fault Zone, *J. Geophys. Res.*, *85*, 6185–6222, doi:10.1029/JB085iB11p06185.

Lachenbruch, A. H., and J. H. Sass (1992), Heat flow from Cajon Pass, fault strength, and tectonic implications, *J. Geophys. Res.*, *97*, 4995–5015, doi:10.1029/91JB01506.

Langbein, J., et al. (2005), Preliminary report on the 28 September 2004, *M* 6.0 Parkfield, California earthquake, *Seismol. Res. Lett.*, *76*, 10–26.

Lee, J. C., J. Angelier, H. T. Chu, J. C. Hu, and F. S. Jeng (2005), Monitoring active fault creep as a tool in seismic hazard mitigation. Insights from creepmeter study at Chihshang, Taiwan, *C. R. Geosci.*, *337*, 1200–1207.

Li, Y. G., J. E. Vidale, and E. S. Cochran (2004), Low-velocity damaged structure of the San Andreas Fault at Parkfield from fault zone trapped waves, *Geophys. Res. Lett.*, *31*, L12S06, doi:10.1029/2003GL019044.

Li, Y. G., P. Chen, E. S. Cochran, J. E. Vidale, and T. Burdette (2006), Seismic evidence for rock damage and healing on the San Andreas Fault associated with the 2004 *M* 6.0 Parkfield earthquake, *Bull. Seismol. Soc. Am.*, *96*, 349–363, doi:10.1785/0120050803.

Lockner, D. A., C. Morrow, D. Moore, and S. Hickman (2011), Low strength of deep San Andreas fault gouge from SAFOD core, *Nature*, *472*, 82–85, doi:10.1038/nature09927.

Marone, C. (1998), Laboratory-derived friction laws and their application to seismic faulting, *Annu. Rev. Earth Planet. Sci.*, *26*, 643–696.

McPhee, D. K., R. C. Jachens, and C. M. Wentworth (2004), Crustal structure across the San Andreas Fault at the SAFOD site from potential field and geologic studies, *Geophys. Res. Lett.*, *31*, L12S03, doi:10.1029/2003GL019363.

Mittempergher, S., G. Di Toro, J.-P. Gratier, J. Hadizadeh, S. A. F. Smith, and R. Spiess (2011), Evidence of transient increases of fluid pressure in SAFOD phase III cores, *Geophys. Res. Lett.*, *38*, L03301, doi:10.1029/2010GL046129.

Moore, D. E., and D. A. Lockner (2011), Frictional strengths of talc-serpentine and talc-quartz mixtures, *J. Geophys. Res.*, *116*, B01403, doi:10.1029/2010JB007881.

Moore, D. E., and M. J. Rymer (2007), Talc-bearing serpentinite and the creeping section of the San Andreas fault, *Nature*, *448*, 795–797, doi:10.1038/nature06064.
Moore, D. E., and M. J. Rymer (2012), Correlation of clayey gouge in a surface exposure of serpentinite in the San Andreas Fault with gouge from the San Andreas Fault Observatory at Depth (SAFOD), *J. Struct. Geol.*, *38*, 51–60.
Mount, V. S., and J. Suppe (1987), State of stress near the San Andreas fault: Implications for wrench tectonics, *Geology*, *15*, 1143–1146.
Murray, J., and J. Langbein (2006), Slip on the San Andreas Fault at Parkfield, California, over two earthquake cycles, and the implications for seismic hazard, *Bull. Seismol. Soc. Am.*, *96*, 283–303, doi:10.1785/0120050820.
Nadeau, R. M., A. Michelini, R. A. Uhrhammer, D. Dolenc, and T. V. McEvilly (2004), Detailed kinematics, structure and recurrence of micro-seismicity in the SAFOD target region, *Geophys. Res. Lett.*, *31*, L12S08, doi:10.1029/2003GL019409.
Nicholson, C., C. C. Sorlien, T. Atwater, J. C. Crowell, and B. P. Luyendyk (1994), Microplate capture, rotation of the western transverse ranges and initiation of the San Andreas transform as a low-angle fault system, *Geology*, *22*, 491–495.
Niemeijer, A. R., and C. J. Spiers (2005), Influence of phyllosilicates on fault strength in the brittle-ductile transition: Insights from rock analogue experiments. High-Strain Zones: Structure and physical properties, *Geol. Soc. London Spec. Publ.*, *245*, 303–327.
Niemeijer, A. R., and C. J. Spiers (2006), Velocity dependence of strength and healing behaviour in simulated phyllosilicate-bearing fault gouge, *Tectonophysics*, *427*, 231–253.
Niemeijer, A. R., C. Marone, and D. Elsworth (2010), Fabric induced weakness of tectonic faults, *Geophys. Res. Lett.*, *37*, L03304, doi:10.1029/2009GL041689.
Ortoleva, P., and W. Chen (1990), Self-organization in far-from-equilibrium reactive porous media subject to reaction front fingering, in *Patterns, Defects and Materials Instabilities*, edited by D. Walgraef and N. M. Ghoniem, pp. 203–220, Kluwer Acad., Dordrecht, Netherlands.
Page, B. M., G. A. Thompson, and R. G. Coleman (1998), Late Cenozoic tectonics of the central and southern Coast Ranges of California, *Geol. Soc. Am. Bull.*, *110*(7), 846–876.
Paterson, M. S. (1973), Nonhydrostatic thermodynamics and its geologic applications, *Rev. Geophys. Space Phys.*, *11*, 355–389.
Powell, R. E. (1993), Balanced palinspatic reconstruction of pre-late Cenozoic Paleogeology Southern California: Geologic and kinematic constraints on evolution of the San Andreas Fault system, in *The San Andreas Fault System: Displacement, Palinspastic Reconstruction and Geologic Evolution*, vol. 178, edited by R. E. Powell, R. J. Weldon, and J. C. Matti, Geol. Soc. Am. Mem., Boulder, Colo.
Powell, R. E., and R. J. Weldon II (1992), Evolution of the San Andreas fault, *Annu. Rev. Earth Planet. Sci.*, *20*, 431–468.
Provost, A. S., and H. Houston (2001), Orientation of the stress filed surrounding the creeping section of the San Andreas Fault: Evidence for a narrow mechanically weak fault zone, *J. Geophys. Res.*, *106*, 11,373–11,386, doi:10.1029/2001JB900007.
Putnis, A. (2002), Mineral replacement reactions: From macroscopic observations to microscopic mechanisms, *Mineral. Mag.*, *66*, 689–708.
Raj, R. (1982), Creep in polycrystalline aggregates by matter transport through a liquid phase, *J. Geophys. Res.*, *87*, 4731–4739, doi:10.1029/JB087iB06p04731.
Ramsay, J. G. (1967), *Folding and Fracturing of Rocks*, 568 pp., McGraw-Hill, New York.
Rathbun, A., F. Renard, and S. Abe (2013), Numerical investigation of the interplay between wall geometry and friction in granular fault gouge, *J. Geophys. Res. Solid Earth*, *118*, 878–893, doi:10.1002/jgrb.50106.
Rice, J. R. (1992), Fault stress states, pore pressure distribution, and the weakness of the San Andreas Fault, in *Fault Mechanics and Transport Properties in Rocks*, edited by B. Evans and T.-F. Wong, pp. 475–504, Academic Press, London.
Richard, J. (2013), Mécanismes de fluage des failles actives: Apport des grands forages et expérimentation de laboratoire, PhD thesis, Univ. of Grenoble, France.
Rubin, A. M., D. Gillard, and J. L. Got (1999), Streaks of microearthquakes along creeping faults, *Nature*, *400*, 635–641.
Rutter, E. H. (1976), The kinetics of rock deformation by pressure solution, *Philos. Trans. R. Soc. London*, *283*, 203–219.
Rutter, E. H. (1983), Pressure solution in nature, theory and experiment, *J. Geol. Soc. London*, *140*, 725–740.
Rutter, E. H., and D. H. Mainprice (1979), On the possibility of slow fault slip controlled by a diffusive mass transfer, *Gerlands Beitr. Geophy., Leipzig*, *88*, 154–162.
Sagy, A., Z. Reches, and I. Roman (2001), Dynamic fracturing: Field and experimental observations, *J. Struct. Geol.*, *23*, 1223–1239.
Schleicher, A. M., B. A. van der Pluijm, J. G. Solum, N. Laurence, and L. N. Warr (2006), Origin and significance of clay-coated fractures in mudrock fragments of the SAFOD borehole (Parkfield, California), *Geophys. Res. Lett.*, *33*, L16313, doi:10.1029/2006GL026505.
Schleicher, A. M., S. N. Tourschervan, B. A. der Pluijm, and L. N. Warr (2009a), Constraints on mineralization, fluid-rock interaction, and mass transfer during faulting at 2–3 km depth from the SAFOD drill hole, *J. Geophys. Res.*, *114*, B04202, doi:10.1029/2008JB006092.
Schleicher, A. M., L. N. Warr, and B. A. van der Pluijm (2009b), On the origin of mixed-layered clay minerals from the San Andreas Fault at 2.5–3 km vertical depth (SAFOD drillhole at Parkfield, California), *Contrib. Mineral. Petrol.*, *157*, 173–187, doi:10.1007/s00410-008-0328-7.
Schleicher, A. M., B. A. van der Pluijm, and L. N. Warr (2010), Nanocoatings of clay and creep of the San Andreas fault at Parkfield, California, *Geology*, *38*, 667–670, doi:10.1130/G31091.1.
Schleicher, A. M., B. A. van der Pluijm, and L. N. Warr (2012), Chlorite-smectite clay minerals and fault behavior: New evidence from the San Andreas Fault Observatory at Depth (SAFOD) core, *Lithosphere*, *4*(3), 209–220.
Siddans, A. W. B. (1972), Slaty cleavage—A review of research since 1815, *Earth Sci. Rev.*, *8*, 205–232.
Sieh, K. E. (1978), Slip along the San Andreas fault associated with the great 1857 earthquake, *Bull. Seismol. Soc. Am.*, *68*, 1421–1448.
Sieh, K. E., and R. H. Jahns (1984), Holocene activity of the San Andreas fault at Wallace Creek, California, *Geol. Soc. Am. Bull.*, *95*, 883–896.
Sleep, N., and M. Blanpied (1992), Creep, compaction and weak rheology of major faults, *Nature*, *359*, 687–692.
Solum, J. G., S. Hickman, D. A. Lockner, D. E. Moore, B. A. van der Pluijm, A. M. Schleicher, and J. P. Evans (2006), Mineralogical characterization of protolith and fault rocks from the SAFOD Main Hole, *Geophys. Res. Lett.*, *33*, L21314, doi:10.1029/2006GL027285.
Solum, J. G., et al. (2007), San Andreas Fault zone mineralogy, geochemistry and physical properties from SAFOD cuttings and core, *Sci. Drill.*, *1*, 64–67, doi:10.2204/iodp.sd.s01.34.2007.
Spencer, J. Q. G., J. Hadizadeh, J.-P. Gratier, and M. L. Doan (2012), Dating deep? Luminescence studies of fault gouge from the San Andreas Fault Zone 2.6 km beneath Earth's surface, *Quat. Geochronol.*, *10*, 280–284, doi:10.1016/j.quageo.2012.04.023.
Steinbrugge, K. V., and E. G. Zachery (1960), Creep on the San Andreas fault: Fault creep and property damage, *Seismol. Soc. Am., Bull.*, *50*, 389–396.
Stewart, M., R. E. Holdsworth, and R. A. Strachan (2000), Deformation processes and weakening mechanisms within the frictional-viscous transition zone of major crustal-scale faults: Insights from the Great Glen Fault Zone, Scotland, *J. Struct. Geol.*, *22*(5), 543–560, doi:10.1016/S0191-8141(99)00164-9.

Tembe, S., D. A. Lockner, and T. F. Wong (2010), Effect of clay content and mineralogy on frictional sliding behavior of simulated gouges: Binary and ternary mixtures of quartz, illite, and montmorillonite, *J. Geophys. Res.*, *115*, B03416, doi:10.1029/2009JB006383.
Thomas, M., J.-P. Avouac, J.-P. Gratier, and J.-C. Lee (2014), Lithological control on the deformation mechanism and the mode of fault slip on the Longitudinal Valley Fault, Taiwan, *Tectonophysics*, *632*, 48–63.
Thurber, C., S. Roecker, H. Zhang, S. Baher, and W. Ellsworth (2004), Fine-scale structure of the San Andreas fault zone and location of the SAFOD target earthquakes, *Geophys. Res. Lett.*, *31*, L12S02, doi:10.1029/2003GL019398.
Titus, S. J., C. DeMets, and B. Tikoff (2006), Thirty-five-year creep rates for the creeping segment of the San Andreas Fault and the effects of the 2004 Parkfield earthquake: Constraints from alignment arrays, continuous global positioning system and creepmeters, *Bull. Seismol. Soc. Am.*, *96*, 250–268, doi:10.1785/0120050811.
Townend, J., and M. D. Zoback (2004), Regional tectonic stress near the San Andreas fault in central and southern California, *Geophys. Res. Lett.*, *31*, L15S11, doi:10.1029/2003GL018918.
Vrolijk, P., and B. A. van der Pluijm (1999), Clay gouge, *J. Struct. Geol.*, *21*, 1039–1048.
Waldhauser, F., W. L. Ellsworth, D. P. Schaff, and A. Cole (2004), Streaks, multiplets, and holes: High-resolution spatio-temporal behavior of Parkfield seismicity, *Geophys. Res. Lett.*, *31*, L18608, doi:10.1029/2004GL020649.
Wallace, R. E. (1970), Earthquake recurrence intervals on the San Andreas fault, *Geol. Soc. Am. Bull.*, *81*, 2875–2890.
Wallace, R. E. (1990), General features, in *The San Andreas Fault System, California*, edited by R. E. Wallace, *U.S. Geol. Surv. Prof. Pap., 1515*, 283.
Weldon, R. J., K. E. Meisling, and J. Alexander (1993), A speculative history of the San Andreas fault in the central Transverse Ranges, California, in *The San Andreas Fault System: Palinspatic Reconstruction and Geologic Evolution*, edited by R. E. Powell, R. J. Weldon, and J. C. Matti, *Geol. Soc. Am. Mem., 178*, 161–198.
Wells, D. L., and K. J. Coppersmith (1994), New empirical relationships among magnitude, rupture length, rupture width, rupture area, and surface displacement, *Bull. Seismol. Soc. Am.*, *84*, 974–1002.
Weyl, P. K. (1959), Pressure solution and the force of crystallization: A phenomenological theory, *J. Geophys. Res.*, *64*, 2001–2025, doi:10.1029/JZ064i011p02001.
Wintsch, R. P., and K. Yi (2002), Dissolution and replacement creep: A significant deformation mechanism in mid-crustal rocks, *J. Struct. Geol.*, *24*, 1179–1193.
Wintsch, R. P., and M. W. Yeh (2013), Oscillating brittle and viscous behavior through the earthquake cycle in the Red River Shear Zone: Monitoring flips between reaction and textural softening and hardening, *Tectonophysics*, *587*, 46–62, doi:10.1016/j.tecto.2012.09.019.
Wood, D. S. (1974), Current views of the development of slaty cleavage, *Annu. Rev. Earth Planet. Sci.*, *2*, 369–400.
Yu, S. B., and C. C. Liu (1989), Fault creep on the central segment of the longitudinal valley fault, eastern Taiwan, *Proc. Geol. Soc. China*, *32*, 209–231.
Zoback, M. D. (2000), Strength of the San Andreas Fault, *Nature*, *405*, 31–32.
Zoback, M. D. (2006), SAFOD penetrates the San Andreas Fault, *Sci. Drill.*, *2*, 32–33.
Zoback, M. D., et al. (1987), New evidence for the state of stress on the San Andreas fault system, *Science*, *238*, 1105–1111.
Zoback, M. D., L. T. Silver, T. Henyey, and W. Thatcher (1988), The Cajon Pass scientific drilling experiment: Overview of phase I, *Geophys. Res. Lett.*, *15*, 933–936, doi:10.1029/GL015i009p00933.
Zoback, M. D., S. Hickman, and W. Ellsworth (2010), Scientific drilling into the San Andreas fault zone, *Eos Trans. AGU*, *91*, 197–199, doi:10.1029/2010EO220001.
Zoback, M. D., et al. (2011), Scientific drilling into the San Andreas Fault Zone—An overview of SAFOD's first five years, *Sci. Drill.*, *11*, 14–28.
Zubtsov, S., F. Renard, J.-P. Gratier, R. Guiguet, D. K. Dysthe, and V. Traskine (2004), Experimental pressure solution compaction of synthetic halite/calcite aggregates, *Tectonophysics*, *385*, 45–57.